Review

A Review of Practical Applications of Fluid Flow and Associated Heat Transfer Modeling in Wellbores

C. Shah Kabir *

Incendium Technologies, Inc., 1700 Bryant Dr., Suite 105, Round Rock, TX 78664, USA; E-Mail: shah@incendiumtech.com

* **Correspondence:** C. Shah Kabir; E-Mail: shah@incendiumtech.com

Academic Editor: Faik Hamad

Abstract

Investigations on two-phase gas/liquid flow in pipes have been under study for nearly six decades. These studies have significantly assisted in managing fluid flow in the wellbore and surface networks, leading to the separation of phases and transmission of oil and gas into the market. This study summarizes some of the main lessons learned in flow through wellbores. Besides understanding some of the fundamental principles, we focused on the practical items of interest: Conventional production scenarios for oil and gas wells; Liquid loading in gas wells; Production in geothermal wells; Heat flow from fluid flow; Transient non-isothermal wellbore modeling; Well blowout in drilling operation; Estimating static geothermal and flowing-temperature gradients in gas wells; Heat mining with fluid circulation in wellbores. Given the diversity of the methods mentioned above, understanding flows in the wellbore and the reservoir becomes equally important. One critical item is the fluid temperature measurement associated with the fluid flow that enables validation of the fluid flow rate, besides revealing information about the reservoir characteristics.

Keywords

Two-phase flow in wellbores; associated heat transfer; applications in wellbore and reservoir;

fluid flow from heat flow; geothermal gradient; thermal energy extraction

1. Introduction

This article presents overall viewpoints and practices of fluid flow and the associated heat transfer in wellbores in many facets of well operations, starting with drilling, production, injection, and reservoir management in the oil and gas field operations. Of course, some of these items are also pertinent to geothermal field operations. Given that the overall approach conveys the evolving nature of fluid flow management in various processes, we do not delve into presenting the associated models and the relevant equations but try to share the overall picture. Contextually, presentations of various field applications became the focal point.

Initially, we introduce mechanistic models of multiphase flow in wellbores that have gained widespread use, followed by their verifications or applications in different field operations. Heat transfer applications for single-phase flow are also highlighted, given the lessons learned and their potential extension to two-phase flow situations. Notably, this aspect has opened the door for harnessing thermal energy by fluid circulation down the annulus and up the tubing in the current energy transition phase. In contrast, drilling operations require a flow of multiple phases, including solids, down the tubing, and up the annulus.

In this two-segment discourse, we first focus on various aspects of multiphase flow problems in different practical settings, followed by those associated with the new lessons learned from the transient-temperature responses, from reservoir characterization to fluid flow-rate estimation to thermal-energy extraction by fluid circulation.

2. Lessons Learned from Fluid Flow Modeling

Studies over several decades helped craft a roadmap for using various evolved models and correlations. Understanding the flow pattern characteristics leading to establishing the flow regimes led to estimating the liquid holdup and pressure drop. As expected, the pipe diameter and well orientation largely influence the flow patterns during multiphase flow. This section briefly overviews some models and their efficacy in actual field settings.

2.1 Flow Patterns in Wellbores and Gauging Models' Performance

The significant difference in pressure and temperature for a producing well along a wellbore suggests that different flow patterns may exist at various depths for a given oil. Increased well-depth results in higher formation temperature and complexity of the multiphase flow, given the increased residence time of fluids. For instance, at the well bottom, only the liquid phase exists below the bubblepoint. As the fluids ascend, methane and ethane gas come out of the solution below the bubblepoint pressure. This reality triggers the bubbly flow. With the upward movement of fluids, initiated by increasing pressure difference, a range of flow patterns may emerge with increased gas production, as Figure 1 illustrates. In oil wells, the gas rate is not high enough for the annular flow, meaning only the bubbly, slug, and churn flow regimes are the norm. The annular flow typically appears in gas/condensate and steam/water production scenarios.
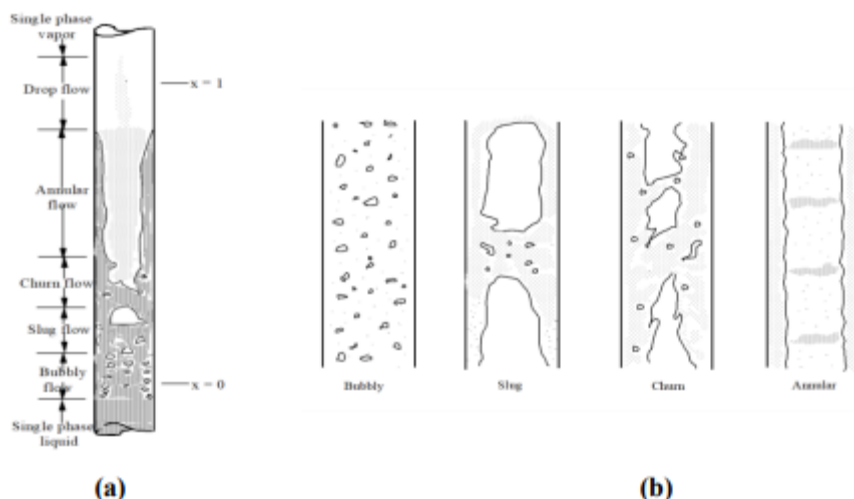
Figure 1 Flow patterns in a vertical upward flow, Collier [1] (a), & flow-pattern delineation, Taitel et al. [2] (b) (After [3]).

Given the evolving nature of the lessons learned over decades, the modern era has adopted mechanistic models involving different flow regimes. However, each method provides somewhat different outcomes. That is because the flow-pattern map and the transition criteria associated with slip between the phases differ. Given that no single model has emerged as a clear winner under various production circumstances, using multiple methods appears pragmatic.

The Ansari et al. model appears justified, given its mechanistic platform and success in field applications while solving steady-state flow problems. Details of the merits of other methods, such as those of Gomez et al. [4] and Kaya et al. [5], appear in Chap. 3 of the Hasan and Kabir book [3]. Nonetheless, multiple models can instill confidence in each field setting. The Ansari et al. [6] model outperforms other models and correlations for gas wells producing gas/condensate and gas/water in annular flow. Gas-lift wells also fall into this category. That said, Hasan and Kabir [7] demonstrated that the simple homogeneous model performs as well as more sophisticated models and correlations in estimating pressure gradients in annular two-phase flow.

To illustrate the points made in the preceding paragraphs, Figure 2 illustrates a field example wherein the pressure-traverse calculations of Ansari et al. (Ans) and the Hasan-Kabir (HK) mechanistic models juxtapose with a field dataset. This 5,151-ft vertical well produces 23 °API dry oil at 1,140 STB/D through a 2.99-in-ID tubing. Given the top-down estimates, discrepancy appears at the well bottom. This error decreases markedly when the computations follow the path of flow direction, that is, bottom up. This observation also implies that enhancing the frictional pressure-drop calculation approach, as done in the Ansari et al. model, is unwarranted for most vertical and near-vertical wells. The use of both laboratory (Ansari et al. [6]) and field (Pucknell et al. [8] and Kabir and Hasan [9]) data tends to support this observation.
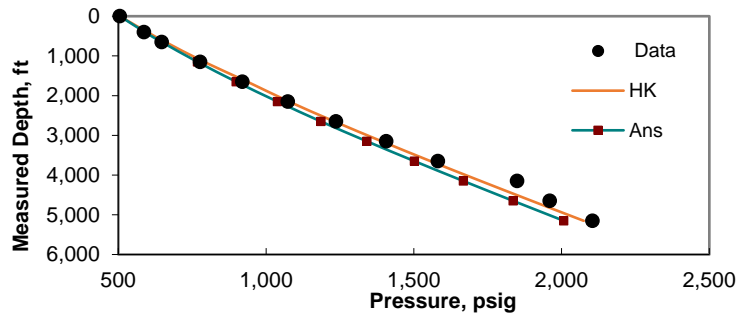
Figure 2 Comparison of mechanistic models with field data (After [3]).

As presented by Hasan and Kabir [3], a small but high-quality dataset from 212 flowing wells compares the performance of some of the commonly used models. These wells have permanent downhole pressure sensors and provide periodic surface rate measurements, and the range of each input parameter appears in Table 1. The models include those of Hagedorn and Brown or HB [10], steady-state OLGA (Bendiksen et al. [11]), Ansari et al. [6], Gomez et al. [4], and the Hasan-Kabir or HK model. Here, the presentation content reflects only partial findings, which appeared in Hasan et al. [12].

Table 1 Range of variables used in the comparative study (After [12]).

Variable	Maximum	Minimum
Liquid Rate, STB/D	27,760	100
Gas/Liquid Ratio, scf/STB	5,615	104
Watercut, %	98	0
Measured Depth, ft	30,650	1,635
Bottomhole Pressure, psig	13,755	108
Wellhead Pressure, psig	10,218	90

The behavior of all tested models appeared very coherent, as exemplified by Figures 3(a) and 3(b). For instance, the fit quality on both of Figure 3 suggests that the data correlate well with the Hagedorn-Brown (HB) method and the Hasan-Kabir (HK) model. Similarly, when we cross-plot computed bottomhole pressures with different models, good correlations appeared, as Figure 4 displays.
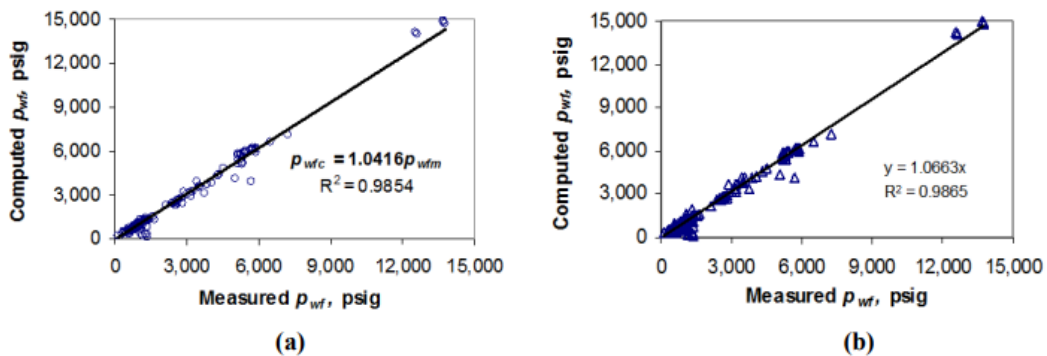

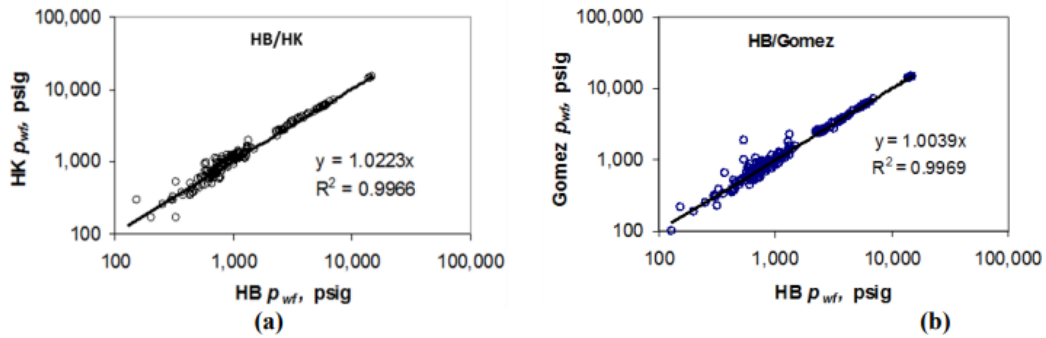**Figure 3** Performance of Hagedorn-Brown correlation (a), and Hasan-Kabir (HK) model (b) (After [12]).

Figure 4 Performance comparison shows good agreement between HB and HK models (a), and HB and Gomez models (b) (After [12]).

2.2 Modeling Approach in Gas/Condensate Wells

In gas/condensate wells, questions arise about the degree of sophistication of the flow model that we need to convert wellhead pressure to bottomhole conditions. Besides, long-term reservoir performance forecasting in a coupled reservoir/wellbore/surface network system needs scrutiny from an overall reservoir management perspective. As it turns out, the use of the homogeneous model, as shown in Kabir and Hasan [13], appears to be a reliable modeling approach for a wide range of gas/condensate ratios, well depths, pressures, and flow rates, as Figure 5 illustrates for three independent datasets. Similarly, the Gray correlation produces reliable results, as Figure 6 demonstrates. Even the well-known Ansari et al. model corroborates these results, as shown in Figure 6.
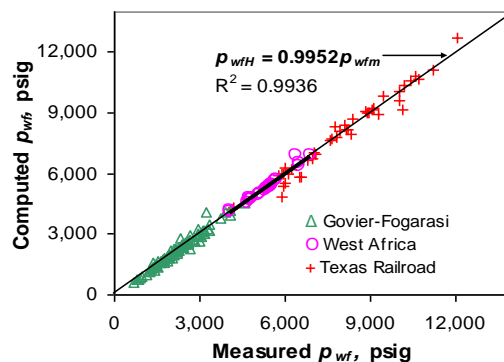

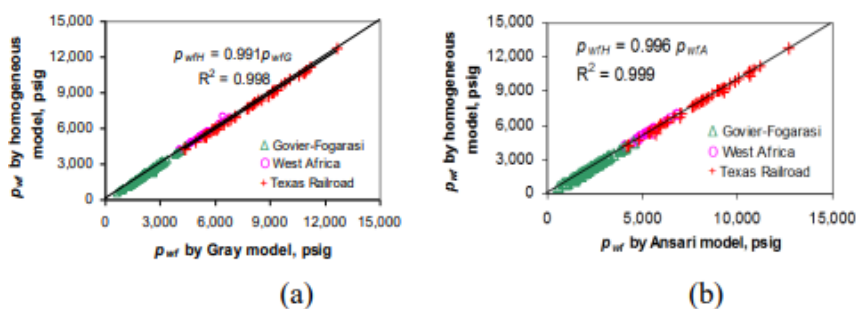**Figure 5** Overall performance of the homogeneous model (After [13]).

Figure 6 Homogeneous model correlates well with the Gray correlation (a), and the Ansari et al. model (b) (After [13]).

The underlying rationale for the Gray correlation [14] and Ansari et al. [6] model converging to the homogeneous model occurs when mist flow appears in gas/condensate systems. Mist flow implies homogeneity of the two phases, which seems to hold for a wide range of bottomhole pressure, condensate/gas ratio, well depth, and flow rate for the three independent datasets, as shown in Table 2. To this end, Figure 6a exhibits an excellent correlation between the homogeneous model and the measured data through bottomhole pressure comparison. Despite the inherent uncertainty in various field data elements, this agreement speaks volumes in the ability of the simplified modeling approach.

Table 2 Range of variables in three datasets (After [13]).

Dataset	p_{wh} psig	p_{wf} psig	Well Depth ft	q_g MMscf/D	CGR STB/MMscf
Texas RRC	3,107– 10,190	4,125– 12,045	7,676– 15,676	0.53–24.9	1.3–193
Govier-Fogarasi	450–2,815	653–4,579	5,939– 12,073	0.67–27.4	1.4–256
West Africa	2,062–4,900	4,076– 6,889	9,454– 13,800	3.71– 30.24	28–131

2.3 Liquid Loading in Gas Wells

Liquid loading arises when the coproduced liquids, condensate, or water becomes a flow obstacle for the gas to lift in the wellbore. With the liquid droplets accumulating at the well bottom, increasing backpressure initiates increasingly higher-pressure loss. This loss in well deliverability triggers a steep decline of the wellhead pressure, leading to the cessation of gas production. This outcome leads to a precipitous drop in the expected gas recovery factor and reserves.

Let us exemplify the problem by showing the transition from the slug to the annular flow in a wellbore, as Riza et al. [15] discussed and shown in Figure 7(a). The corresponding hydrostatic and frictional pressure gradient components for this flow system appear in Figure 7(b). Given the dominance of slug flow, we have not displayed the accelerational pressure gradient for its marginal contribution. As expected, the hydrostatic pressure gradient is the most significant contributor to the total pressure gradient. In annular flow, the frictional head reduces because of the gas-volume fraction (fg) increase, leading to a steep decline in the mixture density.
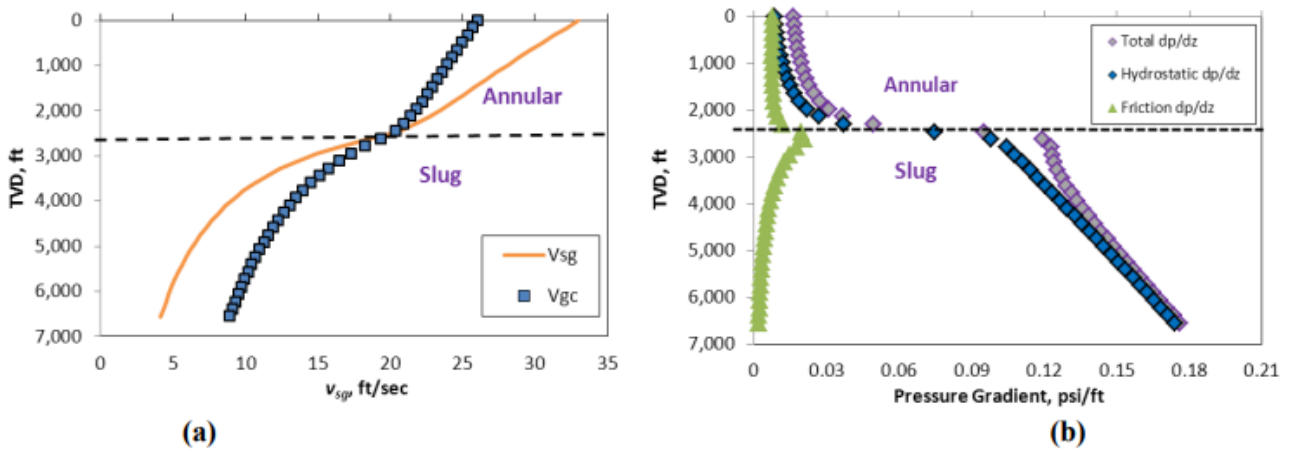
Figure 7 Gas velocity and critical transition velocity profiles (a) indicate the effect of flow regime on pressure gradients (b) (After [15]).

Figure 8a shows how the water/gas ratio (WGR) impacts the transition of the two-phase flow regime, whereas Figure 8b displays the same for the frictional head. A change from annular to slug flow initiates the liquid holdup. Interestingly, the absolute value of WGR does not appear significant for the flow pattern transition. Given that the gas entrains the liquid, the frictional head is more dominant than the hydrostatic head.
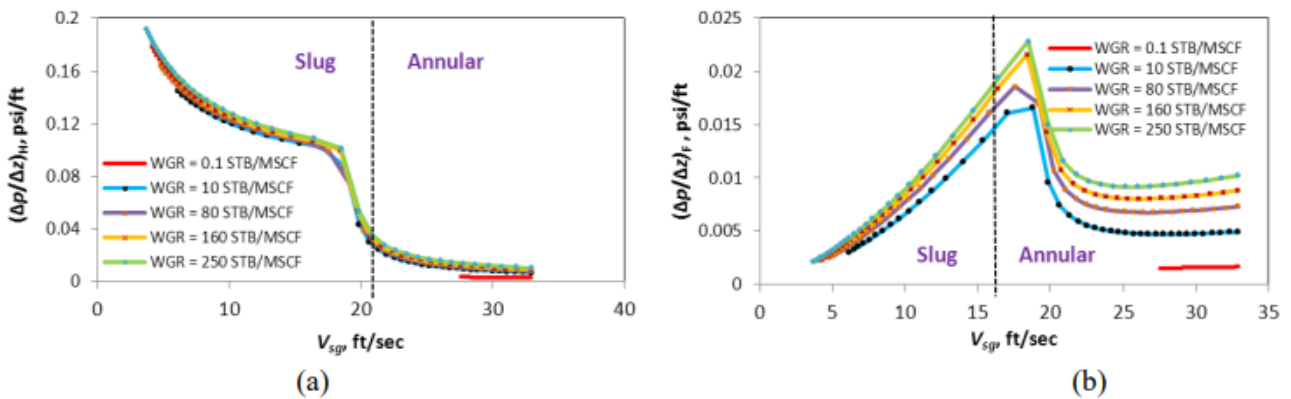

Figure 8 WGR marginally influences the hydrostatic head (a), but significantly influences the frictional head (b) (After [15]).

The Coleman et al. [16] dataset validated the modeling approach as espoused here. All 55 wells in this dataset were liquid loaded. The authors used the original Turner droplet velocity expression to calculate the critical loading velocity for low-wellhead pressure and low-rate gas wells. The relationship between the critical liquid-loading rates vs. the actual liquid-loading gas rate, q_{test} appears in Figures 9a and 9b. Of 55 liquid-loaded gas wells, 51 developed slug or churn flow at the bottomhole. The four data points the proposed approach missed turned out to be close to the critical churn/annular transition line. Overall, the proposed method correlates well with Coleman's data set.
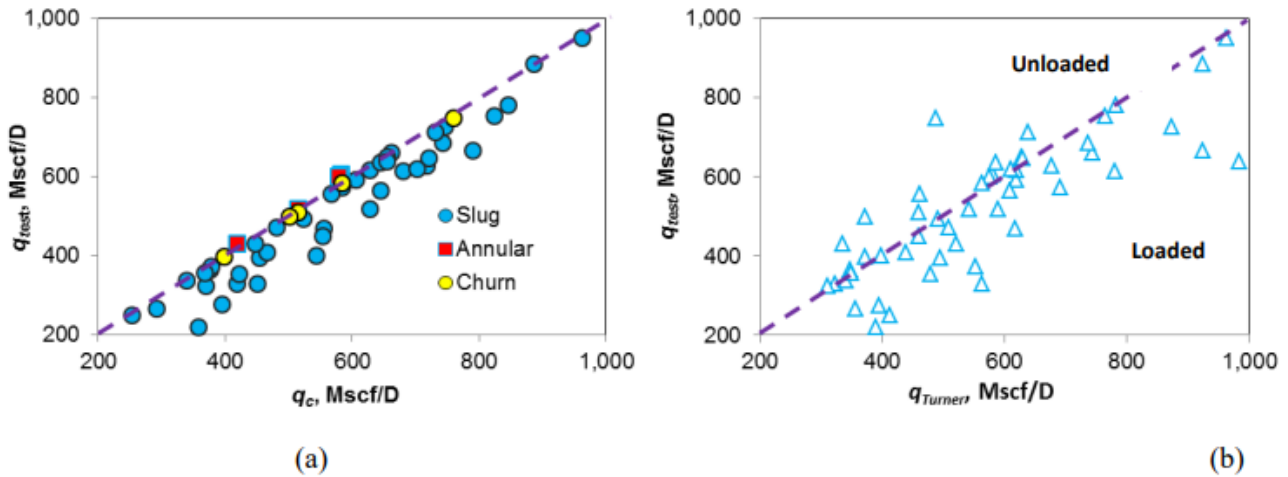
(a)   (b)

Figure 9 Relationship of actual loading rate (q_{test}) with critical annular-churn transition rate (q_c) suggests a good correlation with the entire wellbore diagnostic approach wherein loaded wells dominate (a). Turner et al. method suggests quite a few unloaded wells (b) (After [15]).

Veeken et al. [17] presented field data from offshore liquid-loaded gas wells. Although the wellbore and reservoir information appear substantial, several critical parameters were missing to calculate the liquid-loading rate. The absence of gas/liquid ratios, fluid densities, well trajectories, and tubular sizes presents considerable challenges in estimating the liquid-loading rate. Nonetheless, with reasonable assumptions, as Figures 10a and 10b show, the Riza et al. [15] method made an essential point in understanding the liquid-loading issue compared to the modified-droplet model of Turner et al. [18]. Specifically, the potential for liquid loading looms in many wells.
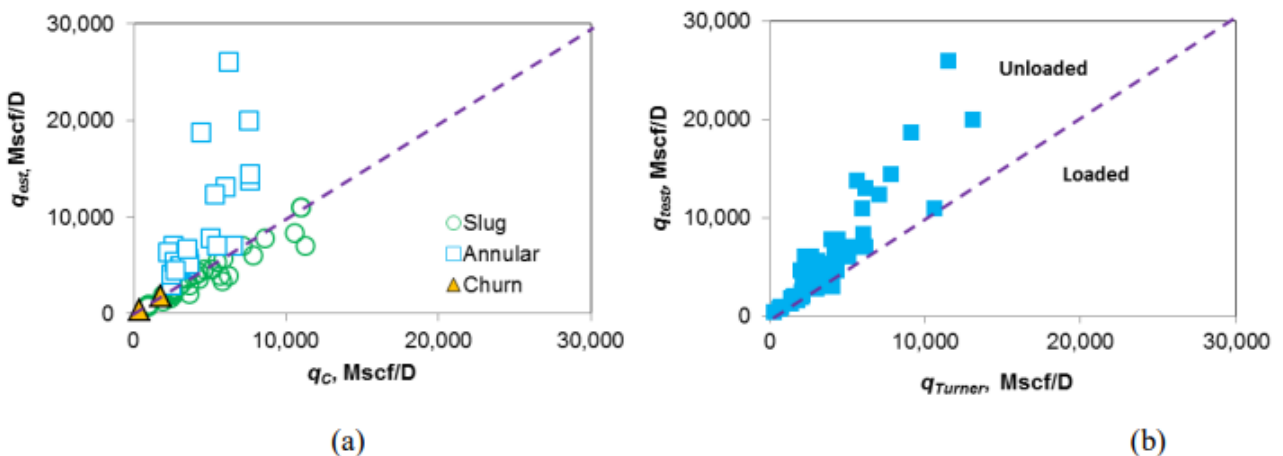

(a)   (b)

Figure 10 Actual liquid-loading rate q_{test} vs. critical annular-churn transition rate q_c indicates wells exhibiting annular flow and those with slug flow (a), whereas the Turner method suggests very few wells with the loading issue (b) (After [15]).

2.4 Lessons Learned

The evolution of model developments over decades produced many two-phase flow models in the oil and gas industry. Nonetheless, the models based on physical principles should take

precedence over those with empirical roots. In field applications, the focus must be on the input data quality, not the model used. For example, a statistical analysis showed that the gas/oil ratio and oil rate become the critical input parameters. In this context, the water rate and oil properties are relatively less influential while estimating the bottomhole pressure with a two-phase flow model.

In gas/condensate wells, mist flow without phase slippage appears realistic in the entire wellbore. This reality suggests that the homogeneous modeling approach is robust for most situations. This reality is supported by Ansari et al.'s mechanistic model and Gray's empirical correlation because they converge to a homogeneous-model formulation. The mist flow occurs with marginal liquid-film thickness on the pipe wall. Like oil wells, no consistent superiority of one method over others prevailed. Nonetheless, models based on the thermodynamics principle should take precedence over those with empirical roots.

Perhaps the critical liquid-loading determination based on an unloaded well experiencing annular two-phase flow throughout the wellbore appears prudent, given that the transition from annular to churn or slug flow triggers the film-flow reversal. This reality necessitates the use of coupled wellbore/reservoir flow modeling for predicting the expected arrival time of this problem.

2.5 Fluid and Heat Flow in Geothermal Wells

The pressure-traverse computation in geothermal wellbores follows a similar trend to that in oil wells, given the commonality of the flow regimes involving bubbly, slug, churn, and annular. Some early studies estimated the slip between steam and water phases with a different model in each flow regime, triggering discontinuity in flow regimes in this hybrid approach. Unlike typical oilfield operations, the sheer number of geothermal wells is a few, and the lack of essential data, such as bottomhole temperature and geothermal gradient, presented a severe challenge to assessing the reliability of pressure-drop assessments.

Some of the earlier studies of Chierici et al. [19], Ambastha and Gudmundsson [20], and Chadha et al. [21] used the hybrid-approach category. Later, Garg et al.'s [22] approach used Duns and Ros [23] flow pattern map and Hughmark's [24] correlation for pressure-drop calculations, with parameters optimized to represent the field data. However, this modeling approach used a constant overall-heat transfer coefficient (U_t), estimated with Ramey's [25] method. Subsequently, Hasan and Kabir [26] showed that improved heat-transfer modeling occurs with the variable-U_t approach, commensurate with variable-tubular diameter.

To illustrate the difference in pressure profiles, Figure 11 presents the pressure profiles for four models for the KE1-22 well, taken from the Garg et al. [22] dataset. In Figure 11(a), H-B represents the Hagedorn-Brown correlation [10], and H-K stands for the Hasan-Kabir model. Interestingly, this example exhibits multiple flow regimes, starting with single-phase water flow at the bottomhole and ending with the annular two-phase flow at the wellhead. The associated heat-transfer calculations with temperature suggested the variability of U_{to} in Figure 11(b), wherein it turned out to be 7.4 Btu/h-ft2-°F at the well bottom and about 10 Btu/h-ft^2-°F at the top. Details of these calculations appear in Hasan and Kabir [5, 26].
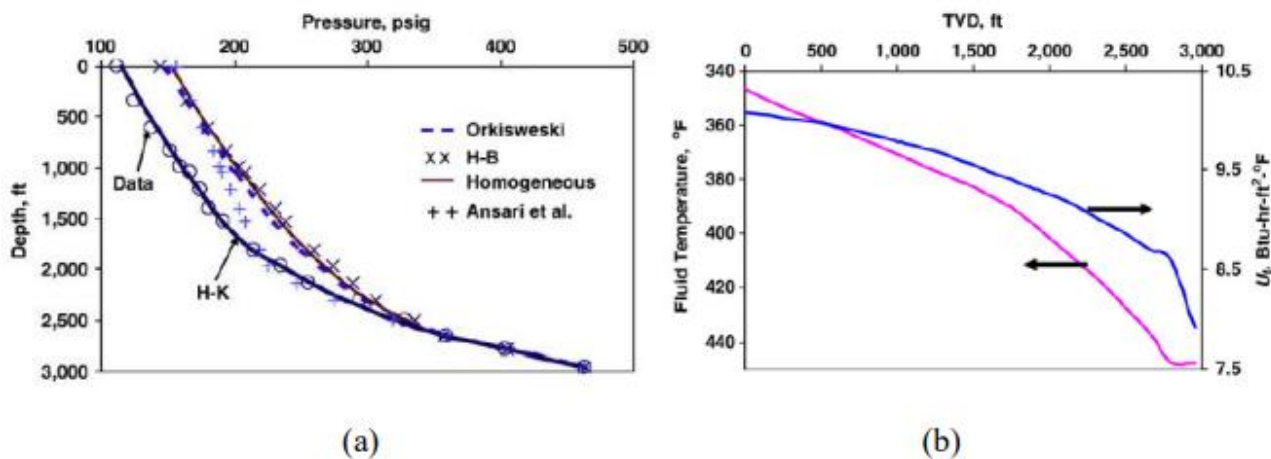
Figure 11 Pressure traverse computation with four models (a), Variable U_t, and fluid temperature profiles (b) for the K-22 well (After [26]).

Overall, the H-K approach [5, 26] showed that the two-phase flow modeling for geothermal wells applies to wells with various orientations and geometry. The associated heat-transfer model ensures the energy balance in the entire wellbore by accounting for variable-pipe diameter, emphasizing convective-heat transport in the annulus. Interestingly, the high-quality Garg et al. [22] dataset showed that all five models studied performed similarly. Nonetheless, the H-K model offers smooth transition boundaries between the flow regimes. Still, one can choose any two-phase flow model to ascertain pressure-drop calculations but needs a credible heat-transfer model to generate the associated temperature profile. More recently, Tonkin et al. [27] provided a comprehensive review of mathematical models for geothermal wells. One can gain insights from this study to learn the strengths and limitations of various models and numerical simulators for both steady-state and transient flow problems.

While modeling the conventional subcritical geothermal fluids can be reasonably straightforward, the wells producing supercritical fluids undergo severe heat loss, significantly reducing the wellhead's fluid temperature. Recently, several studies have emerged to address this critical issue as interest grows in this domain in the quest for renewable energy. To that end, Battistelli et al. [28] used TOUGH2's extended version of the coupled wellbore/reservoir model to simulate a few field cases published previously.

Specifically, the authors presented two wells: (1) Well KD-13 of the Kizildere field in Turkey with a low NaCl content (20,000 ppm) but with high dissolved CO_2 (20,000 ppm); (2) Well W2 from an unidentified field operated by ENEL that produces very high NaCl (9,600 ppm) and CO_2 (30,000 ppm). Figure 12 suggests a high-quality match with field data for two extensions of the TOUGH2 simulator, EWASG, and EOS2H. Then, the authors compared the solutions with an unpublished simulator, PROFILI, for another well, IDDP-1, as shown in Figure 13. These model validations under supercritical steam-like conditions indicate that we can exploit magmatic heat sources for harnessing thermal energy.
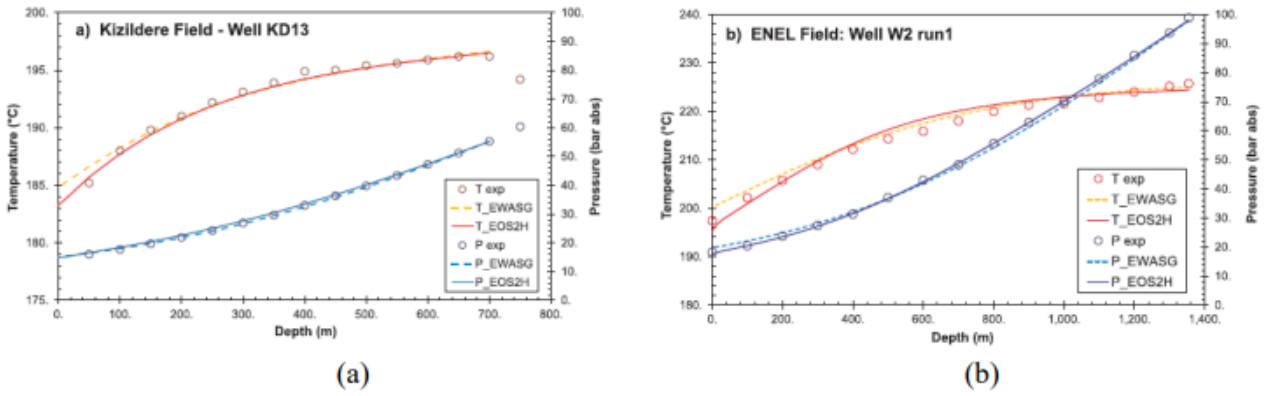
Figure 12 Simulated pressure and temperature vs. depth: (a) Well KD13; (b) Well W2. T@Well-EOS2H vs. T2Wll-EWASG. (After [28]).
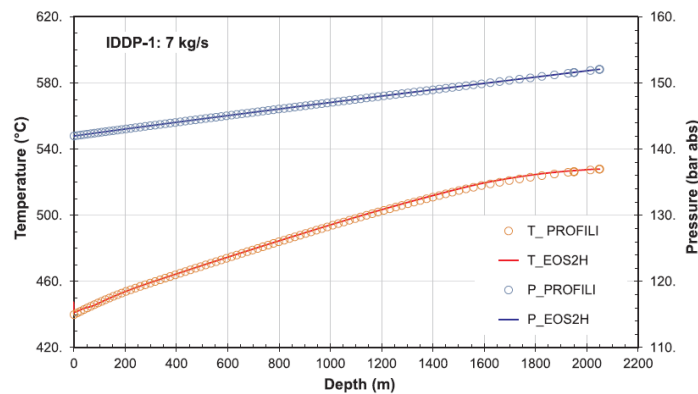

Figure 13 Simulated pressure and temperature vs depth for Well IDDP-1: T2Well-EOS2H vs. PROFILI comparison (After [28]).

2.6 Modeling Steam-Injection Wells

Given the high inherent viscosity, steam injection in heavy and extra-heavy oil reservoirs becomes necessary. Steam-assisted gravity drainage, or SAGD, has been common in this setting since the 1980s, such as in Alberta, Canada, wherein the world's third largest heavy-oil reserves exist. Most recently, Jamshid-Nezhad [29] showed that steam alternating non-condensable gas injection significantly supersedes the conventional SAGD process. Historically, Ramey's pioneering simplified analytical model [25] for estimating the fluid temperature in the reservoir using the temperature-diffusivity equation paved the way for an initial assessment. Satter [30] extended Ramey's steam injection method by considering steam condensation and treating heat loss as a time-dependent function.

Subsequently, Willhite [31] proposed a methodology for estimating the heat-transfer coefficient using the inner tubing, casing, and the cement bond between the casing and the formation. This approach has remained the bedrock of the industry. Pacheco and Farouq Ali [32] presented a modeling approach for calculating the pressure drop and steam quality profile in a steam injection well. Their model involved energy and momentum balance expressions for generating wellbore heat transmission. Also, Farouq Ali [33] presented another comprehensive wellbore model for steam injection and geothermal applications. A subsequent wellbore modeling approach by Fontanilla and

Aziz [34] estimated the pressure and steam quality variation as a function of depth. More recently, analytical models have appeared in SAGD performance assessment, as articulated by Zargar and Farouq Ali [35, 36].

Despite the abundance of analytical models, You and Rahnema [37] have recently proposed a fully implicit numerical model for estimating steam quality, temperature, and pressure profiles in a vertical steam injection well—the refined grids aid in solving a system of differential equations with the Newton-Raphson method. The mass, momentum, and energy balance equations underpin this solution approach. This formulation approach allows for managing both unsteady-state and steady-state steam injection processes. Figure 14 sketches the model's content. The results of the forward modeling, attempting to replicate the field of pressure and steam quality, appear reasonable compared to some of the existing models of Fontanilla and Aziz [34] and Bahonar et al. [38], as Figure 15 and Figure 16 illustrate. Overall, models of this nature unravel pertinent information about changes in pressure, temperature, and steam quality, leading to well design and management of production operations.
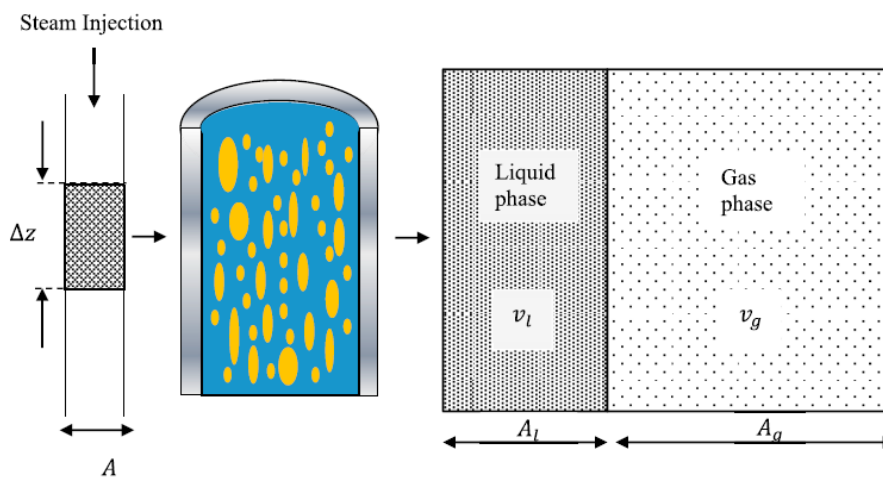

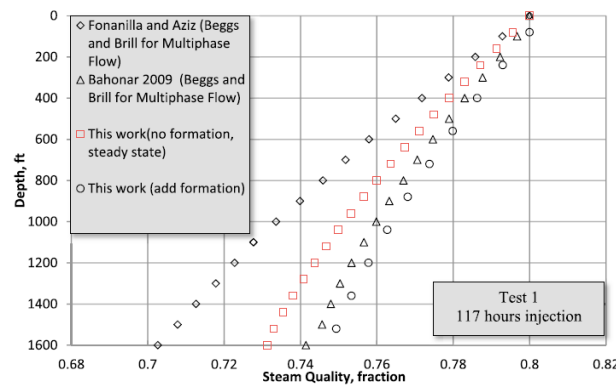**Figure 14** Steam injection in a wellbore (After [37]).

Figure 15 Comparison of model performances for steam quality in injection profiles after 117 h injection (After [37]).
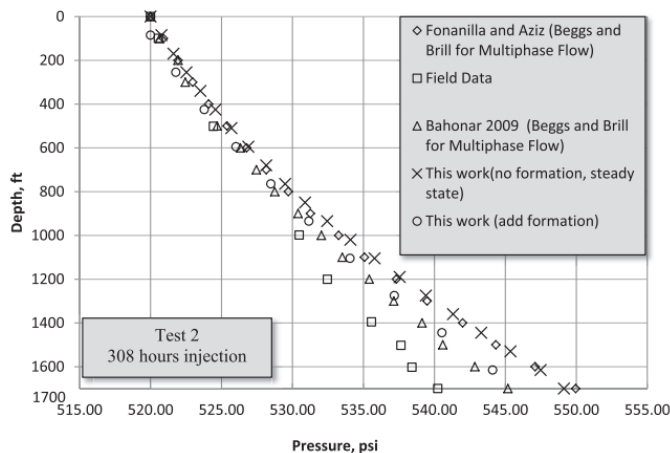
Figure 16 Comparison of model performances for wellbore pressure profiles after 308 h of steam injection (After [37]).

Most recently, Zhao et al. [39] proposed a new numerical model for simulating wellbore fluid flow and heat transfer for supercritical water injection in a wellbore. The authors used a numerical solution of the two-dimensional unsteady heat-conduction equations. A new modified correlation of frictional coefficient appeared and the unsteady heat loss to the formation was directly calculated. Field data helped validate the model's efficacy in which the relative errors of wellbore fluid pressure and temperature appeared to be less than 1%.

2.7 Managed Pressure Drilling & Well Blowouts

During a drilling operation, good pore pressure and reservoir inflow estimations during a gas kick incident become necessary for retaining safety margins. Methods relying on downhole measurements and petrophysical information become challenging in real-time operations. To mitigate these operational challenges, Ambrus et al. [40] offered a model-based estimation technique for a Managed Pressure Drilling (MPD) system that uses surface measurements. A simplified transient drift-flux model (DFM) underpins this MPD modeling approach. This model captures essential dynamics during a gas kick with reduced-order computational overhead but retains modeling accuracy.

Figure 17 presents the flow diagram for Ambrus et al.'s methodology, wherein the upward flow occurs in the annulus. Figure 18 compares the model results with the mud flow rate and pit gain data, showing a match of reasonable accuracy. When the model's data is compared with the well-known transient model OLGA, the overall outcome appears very encouraging, as Figure 19 suggests.
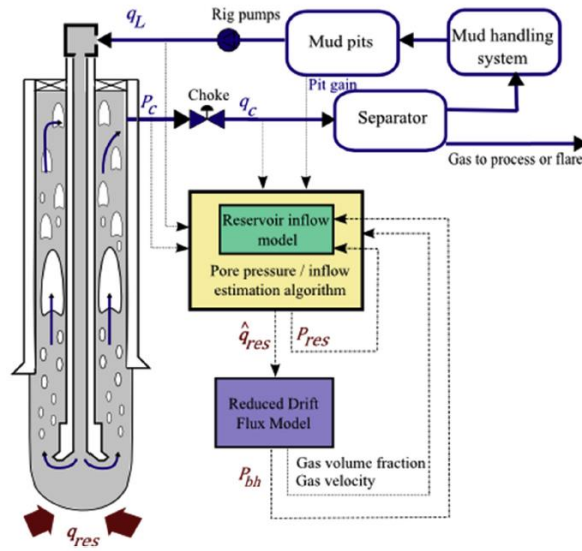
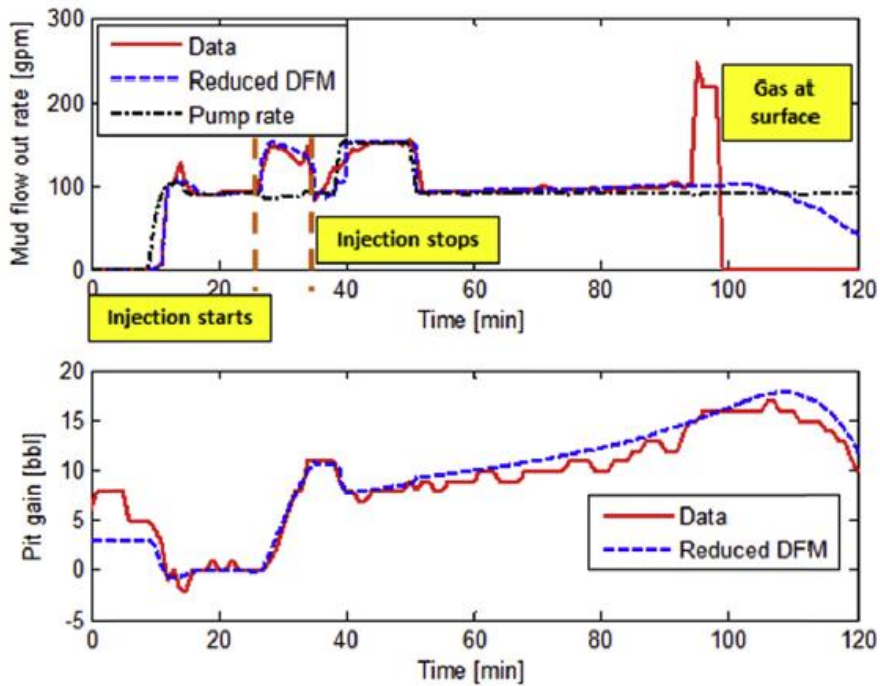**Figure 17** Flow diagram of the proposed methodology (After [40]).

Figure 18 Experimental data comparison with reduced DFM; pit gain (lower) and mud flow rate out (upper) (After [40]).
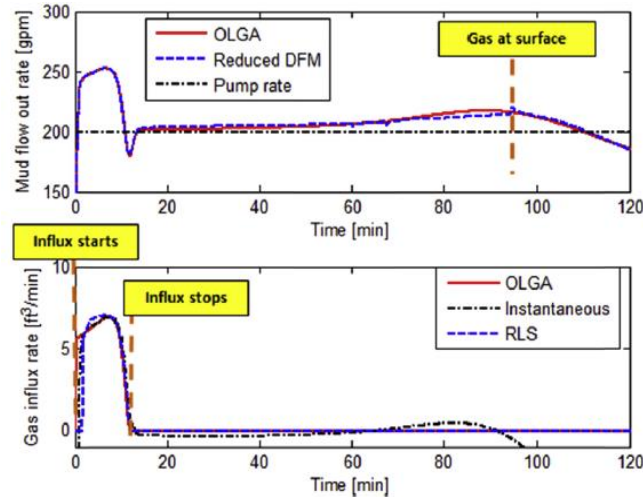
Figure 19 Mud flow rate from OLGA and matched with reduced DFM (upper); gas influx rate (lower) (After [40]).

Overall, this study found that the two-phase flow model consists of a transport equation governing the gas flow dynamics representing pressure dynamics in response to changes in choke opening. This reduced-order DFM captures the essential two-phase dynamics during a gas kick that becomes suitable for real-time operations. Actual field data provided the model's validation that OLGA verified. In addition, the surface sensor measurements and non-interference with well-control procedures provide an advantage over other operations. Subsequently, Xu et al. [41] offered a transient non-isothermal two-phase flow model for handling a gas-kick situation.

2.8 Estimating Discharged Volume in Uncontrolled Gas and Oil Wells

2.8.1 Managing Gas Well Blowout

A well can go out of control during a drilling operation due to a lack of significant system flow barriers. For instance, when an unexpected over-pressured reservoir interval or pressure management issue appears, ample reservoir fluids can spill, causing severe safety hazards for the drilling rig and the operational personnel involved. This section sketches a practical gas or oil spill-risk assessment method articulated by Liu et al. in gas [42] and oil [43] wells with coupled wellbore/reservoir modeling. The method is anchored in unsteady-state two-phase fluid flow and heat transfer modeling from the reservoir to the spill point; the statistical design of experiments helped study the relative importance of some of the independent variables. Although we present a probabilistic study of gas wells, Macondo's 2010 oil spill in the Gulf of Mexico becomes the focal point of this discourse, given that many industry experts provided their independent results of the spilled oil volume. However, before delving into the oil scenario, let us discuss the gas blowout situation.

Figure 20a displays the time-dependent wellbore temperature profile due to choked flow at the wellhead. Although the fluid temperature declines in its flow path while moving up, it does increase over time. This increase in temperature holds up despite the blowout rate decline due to reservoir depletion. Two essential components of heat transfer, kinetic energy (KE) and Joule-Thompson (JT) effects, come into play, that Figure 20b illustrates. The significant decline in fluid temperature at the

wellhead originates from the extreme expansion of gas that precipitates a rapid decline of the pressure gradient near the wellhead. This reality significantly increases the KE at the expense of internal energy contribution, leading to a rapid decline of fluid temperature near the wellhead. Of course, the J-T cooling effect considerably shifts the actual temperature profile to the left.
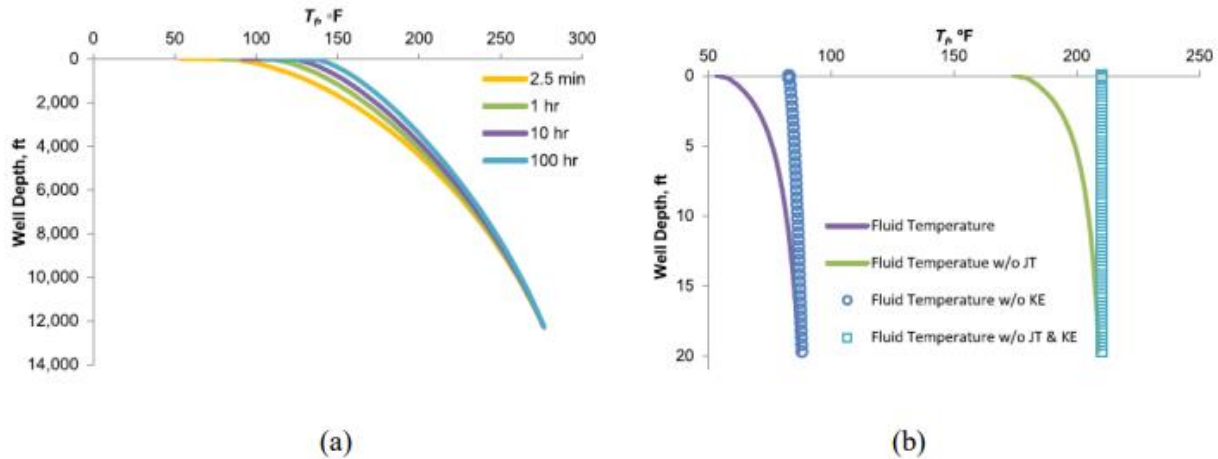

Figure 20 Fluid temperature in the wellbore during a blowout event (a), fluid temperature profile near wellhead after 2.5 min considering JT and KE effects (b) (After [3]).

A probabilistic simulation approach helped understand the various reservoir parameters influencing a blowout situation. Table 3 presents the range of four independent variables in this three-level design. Figure 21a presents the low, medium, and high-level cases, reflecting the range of each independent variable for a blowout period of 300 days. This folded-Plackett-Burman design includes both nonlinearities and interactions between the variables and quantifies the significance of each independent variable. However, for realistic scenario analysis, the dependent variable of cumulative production loss during a 100-day blowout became the focal point. As Figure 21b shows, permeability, and formation thickness, meaning reservoir conductivity, became the most crucial variable in the cumulative fluid loss. Liu et al. [5, 42] also discussed how jet fire and flammable gas hazards could be quantified during a gas well blowout.

Table 3 Reservoir parameters with uncertainties for the blowout model (After [3]).

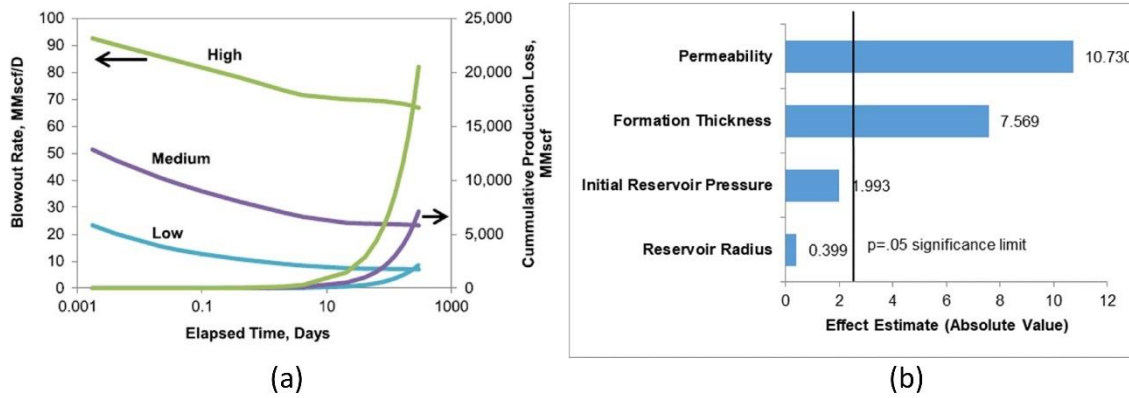|	Low	Medium	High
Formation thickness, ft	50	100	150
Initial reservoir pressure, psia	5387	5985	6584
Reservoir radius, ft	2952	3280	3608
Permeability, md	1	2.3	5

(a)

(b)

Figure 21 Probabilistic blowout behavior for a given case (a), Pareto chart ranks the variables impacting the spilled volume (b) (After [3]).

2.8.2 Managing Oil-Well Blowout

This section discusses a pragmatic approach to oil-spill risk assessment. A coupled analytical reservoir/wellbore modeling approach underpinned the fluid flow and the associated heat transfer phenomena, followed by the uncertainty analysis for assessing the spilled fluid volume. Two-phase gas/oil flow in a wellbore with changes in flow patterns coupled with unsteady-state reservoir depletion became implicit in this analytical modeling approach. This model aided in estimating the Gulf of Mexico's 2010 Macondo oil spill in a probabilistic frame, as described by Liu et al. [43], which was validated by the results of other subject-matter expert studies. Depicting the risk picture of the uncontrolled wellbore flow events and combining the physical model with distributions of uncertain parameters enabled volumetric estimation of a range of spilled volumes. Figure 22 displays simulated cases of the evolution of gas-volume fraction in two-phase flow and the associated flow regimes in three permeability cases throughout the wellbore at early times.
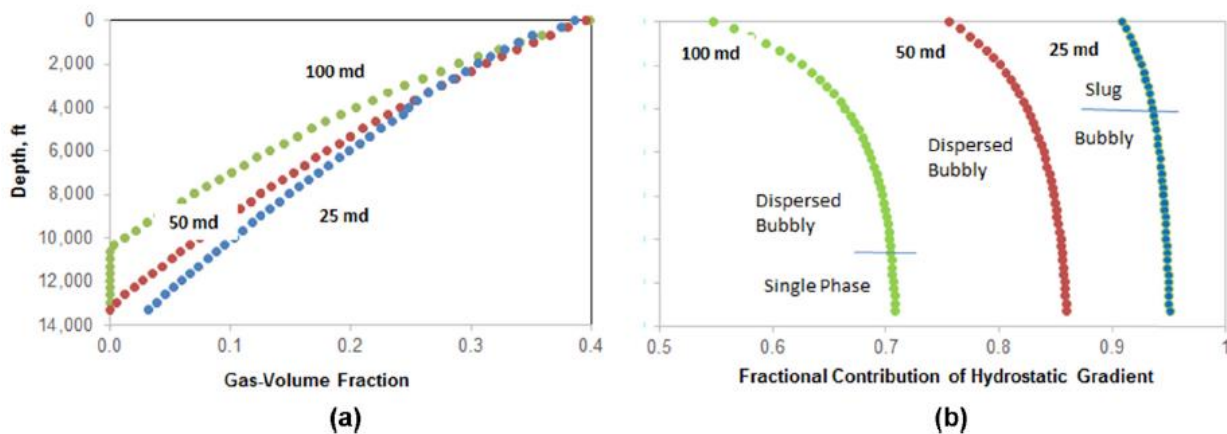

Figure 22 Gas-volume fraction distribution in the wellbore (a) and corresponding hydrostatic pressure gradient (b) contribution for three different permeability reservoirs (After [43]).

Figure 23 presents a conceptual schematic of this case study's wellbore/reservoir system, as shown in the Oldenburg et al. [44] study. Without hard data, this section presents the range of scenarios with discharge rate and other significant independent variables. Figure 24, presenting

some of the potential blowout scenarios and their assessment, aids in sketching the probability distributions for the uncertainty range of independent variables. The sum of the probability associated with each scenario equals one. In the Macondo case, the available information in the open literature constituted the required content. Liu et al. [44] summed up the discharged volume product and its probability of obtaining the well-specific blowout risk. This solution approach led to barrier effectiveness and risk-reduction studies.
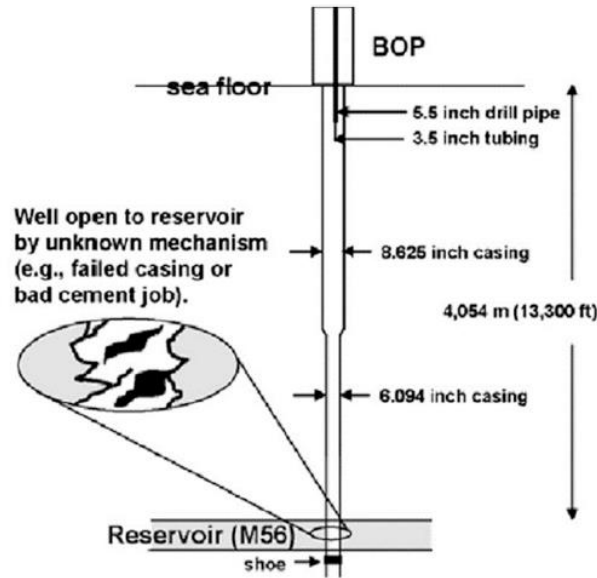
Figure 23 A schematic representation of the Macondo wellbore (After [44]).
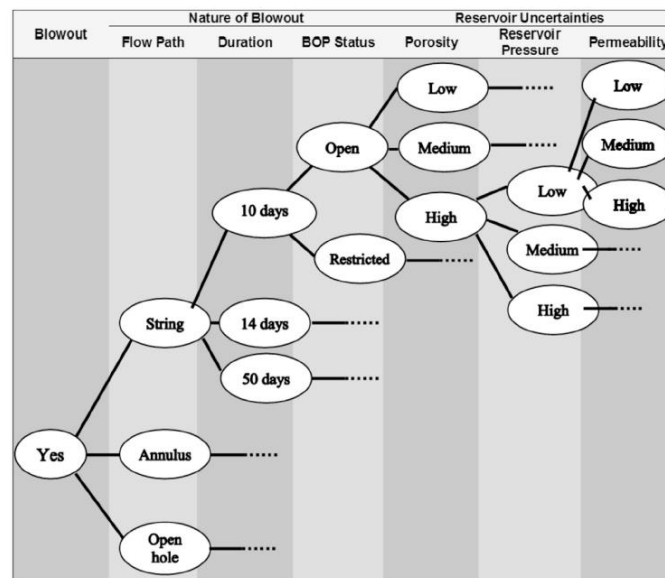

Figure 24 Risk and uncertainty assessment in a blowout scenario (After [43]).

Figure 25a displays the Pareto chart for the discharged volume, the dependent variable. All five variables appear consequential because they exceed the 95% confidence interval line. On a Pareto chart, the x-axis represents the student's t-values, and the y-axis contains the independent variables. Interestingly, the negative value associated with the BOP restriction implies that its

increase hurts the dependent variable, discharged volume. The cumulative distribution function (CDF) for the 17 runs appears in Figure 25b, with the most probable or p-50 outcome for the total discharged volume of 3.8 MMSTB, with an uncertainty range of 2.9 and 4.7 MMSTB. A follow-up study provided a comparative picture of the p-50 outcome with those of subject-matter experts in this domain, as shown in Figure 26. One of the critical takeaways is that strengthening the blowout risk by allocating safety barriers can mitigate risks, given that the reservoir-centric variables remain unknown.
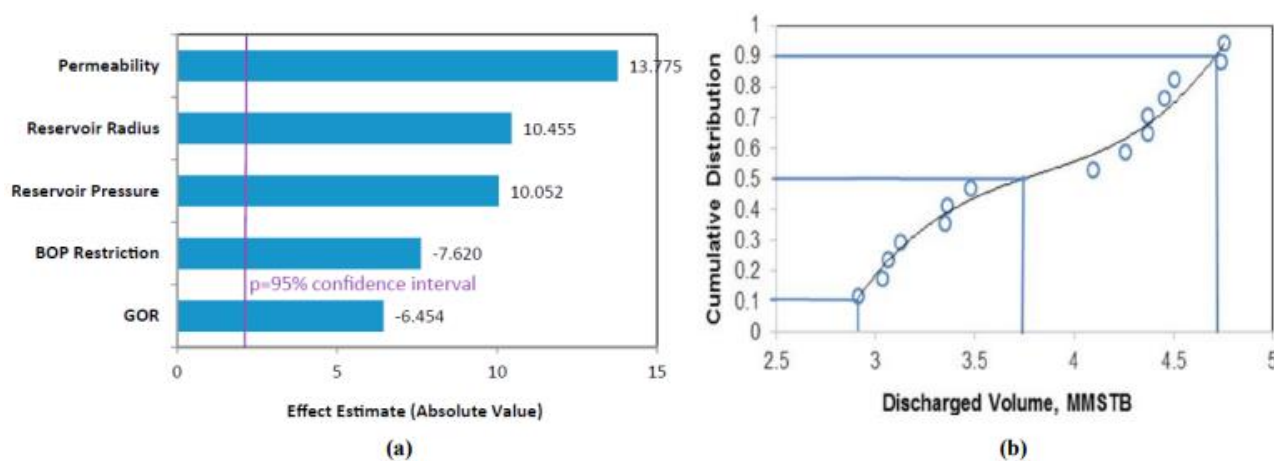

Figure 25 Pareto chart for the five-variable Macondo study (a), CDF of the discharged volume (After [43]).
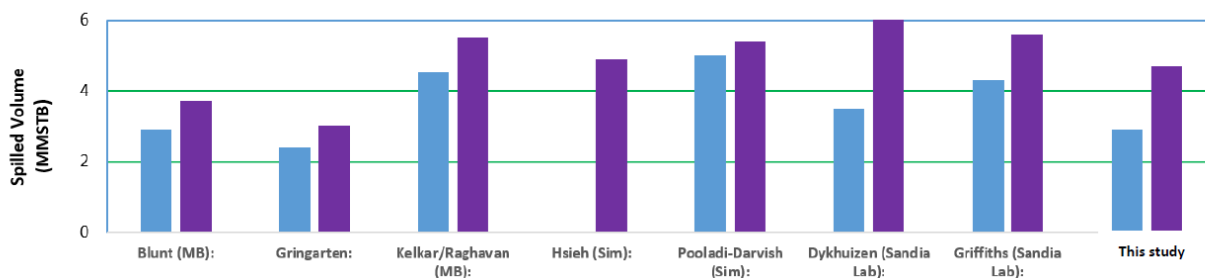

Figure 26 Blind test results of various experts for the possible range of spilled volume.

This Macondo well incident has gained so much attention that studies continue related to various elements well after a decade. Stress evolution related to wellbore integrity by Michael and Gupta [45] and time-variant release of oil and gas mixture in the water involving oil-droplet size distributions by Spaulding et al. [46], are a few in a plethora of studies, particularly those in marine biology.

3. Lessons Learned from Transient Temperature Modeling

3.1 Modeling Wellbore Fluid Flow and Heat Transfer During Transient Testing

Given that the changes in fluid compressibility distort the early-time response in a pressure-transient test, both flow and shut-in tests require identifying and discarding that period for a meaningful analysis, leading to reservoir information. Beyond addressing this point, this section

shows how one can estimate fluid flow rates from wellbore temperature data, both at a single point and using a distributed sensor. Lastly, we discuss how fluid and heat flow rates can be assessed from each other, leading to meaningful information.

Constitutive equations involving mass, momentum, and energy balances and the fluids' pressure/volume/temperature (PVT) relation provide the foundation for dealing with pressure transient analysis; Figure 27 sketches the basis for a control volume of unit length within a wellbore. Details of this modeling approach appear in Hasan et al. [47].
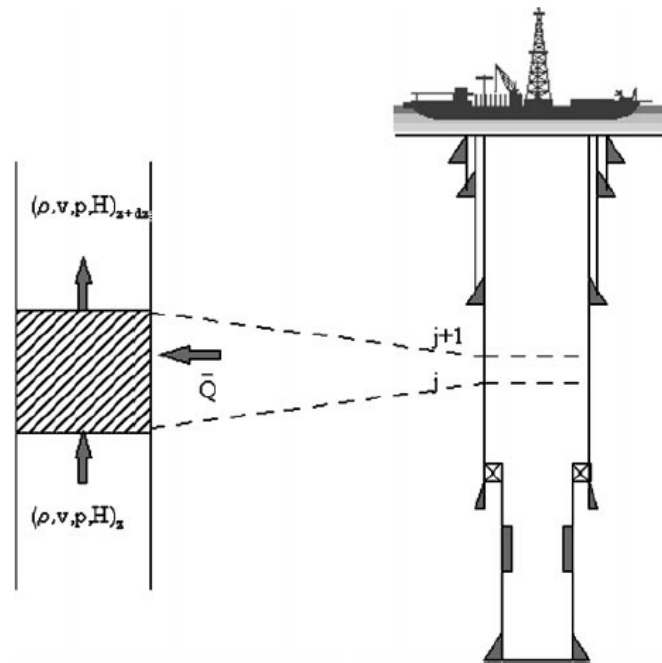

Figure 27 Mass, momentum, and energy balance in an oil well (After [47]).

The field test involves a 24-hour flow period, followed by about 99 hours of shut-in. Pressure and temperature sondes measure about 200 ft above the perforations. Figure 28 depicts the changes in both the gas volume fraction and fluid density at three-time intervals in this 10,000 ft well during a drawdown test. During this transient flow period, the gas occupies a larger pore volume within the wellbore with increasing time until attaining a steady flow rate at the surface. Figure 29 shows that the storage period lasts about 0.2 hours before the derivative plateau appears for both the drawdown and shut-in periods. Then, one can estimate the reservoir permeability and skin. As expected, the drawdown response has somewhat lower storage than the buildup.
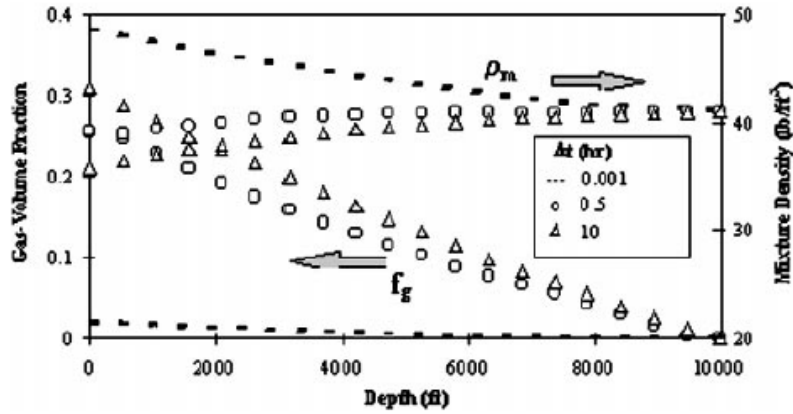
Figure 28 Changing gas volume and mixture density during a buildup test (After [47]).
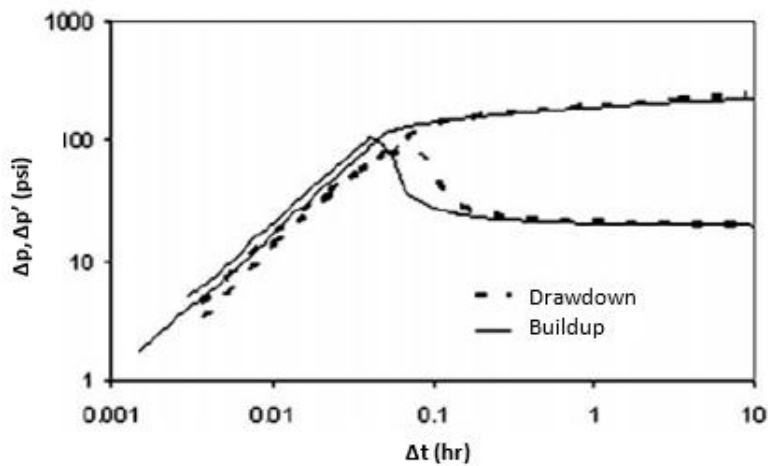

Figure 29 Reduced storage effect during a buildup test (After [47]).

Subsequently, this test involved a production period of 24 hours, followed by a 99-hour pressure-buildup test. Figure 30 displays the pressure and temperature match, both downhole and at the wellhead. The temperature mismatch during production is related to the offset gauge 200 ft above the fluid entry point. Nonetheless, the overall match of pressure and temperature profiles appears satisfactory.
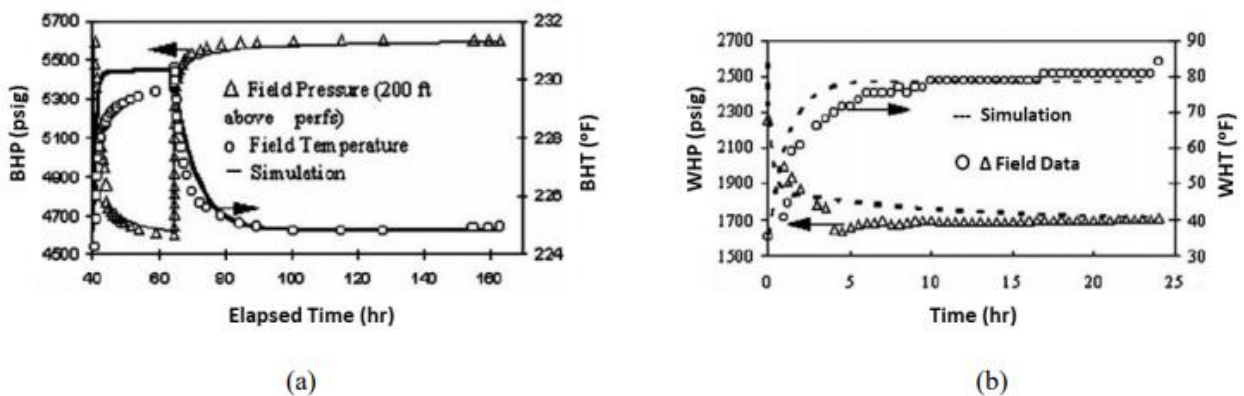

Figure 30 Matching bottomhole pressure (BHP) and temperature (BHT) and (a) wellhead pressure (WHP) and temperature (WHT) by forward simulation (b) (After [47]).

Some of the key takeaways from the lessons learned for the model validation with field data in an offshore environment are that: (a) a transient two-phase fluid and heat flow modeling approach appears satisfactory, (b) decreasing storage behavior during the shut-in period is expected because of wellbore fluid compression.

3.2 Rate Estimation with Temperature and Pressure Data: Single- and Multi-Station Approach

Given that flow metering accuracy is not exemplary as temperature and pressure measurements, estimation of this item becomes a vital interest. We discuss how high-frequency temperature measurements can ascertain fluid flow rate in this context. To that end, we present examples from gas and oil wells from a single-point measurement at the wellhead, followed by multipoint measurements along the wellbore for gas wells.

3.2.1 Multirate Gas-Well Test

Izgec et al. [48] provided the required data of a 20,000 ft well for a vertical gas well in a high-temperature reservoir on the U.S. Gulf Coast. A multi-rate test provided the required pressure and temperature data at the bottomhole and wellhead. This study used the single-point method at the wellhead and the multipoint method involving the data at the wellhead and bottomhole. Figure 31 demonstrates that the transient wellhead temperature in an increasing flow-rate sequence matched in rate computation.
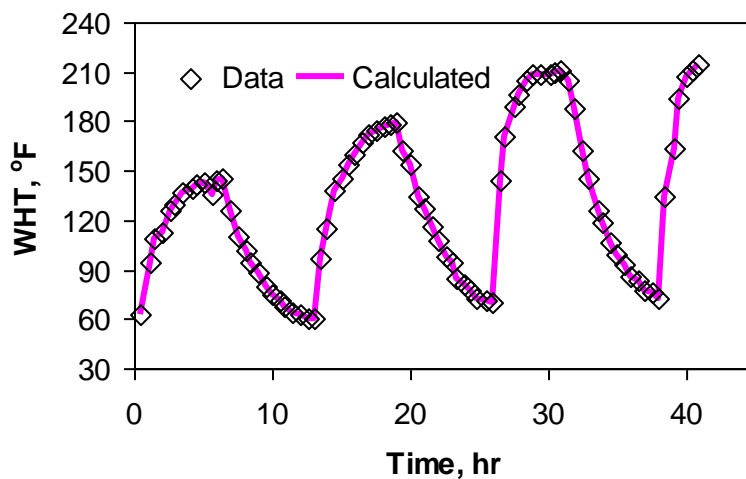
Figure 31 Matching WHT with the single-point method (After [48]).

The resultant rate computational results appear in Figure 32 with the two computational methods. As expected, the entire wellbore approach captured the transient nature of the rate, as opposed to the single-point approach in a 0.35 md permeability system of significant depth. The authors noted that ±5°F temperature error at the wellhead translates into 3 to 7% error in flow rate, thereby assuring the method's reliability.
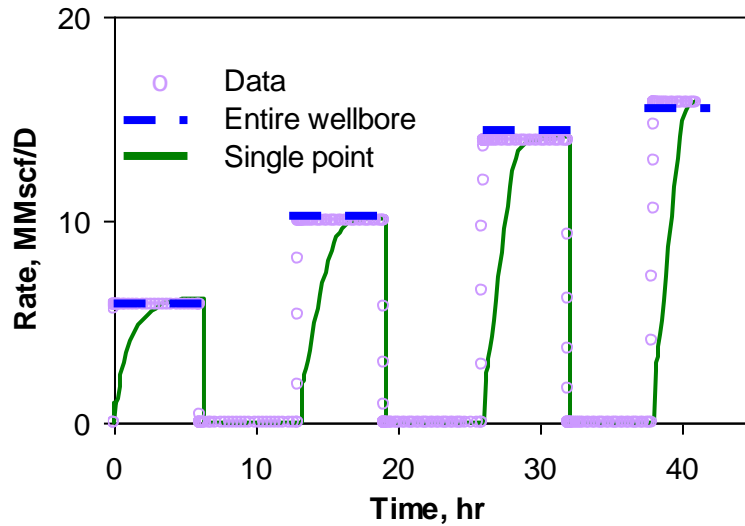
Figure 32 Comparing measured and computed rates with both methods (After [48]).

3.2.2 Tahiti Multirate Oil-Well Test

As Izgec et al. [48] discussed, a combined cleanup and shut-in period of about 70 hours preceded the variable-rate test, which spanned 60 hours in this deepwater setting. Given the transient nature of the flow problem, the single-point approach provided the rate estimation. Figure 33 presents the wellhead temperature data measured at 9,600 ft MD, whose reservoir depth is 26,500 ft MD. The quality of temperature match assures a reliable rate history outcome. However, as Figure 34 shows, the temperature derived matches the measured values well, except for those at the highest rates. In this setting, physical limitations at surface rate metering capability required that the rate exceeding 9,000 STB/D needed diverting to another vessel. There, issues surfaced with rate metering, leading to this discrepancy.
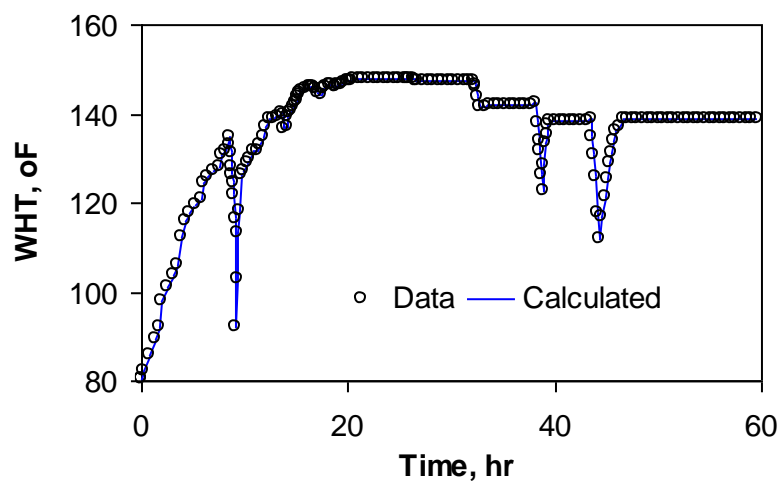

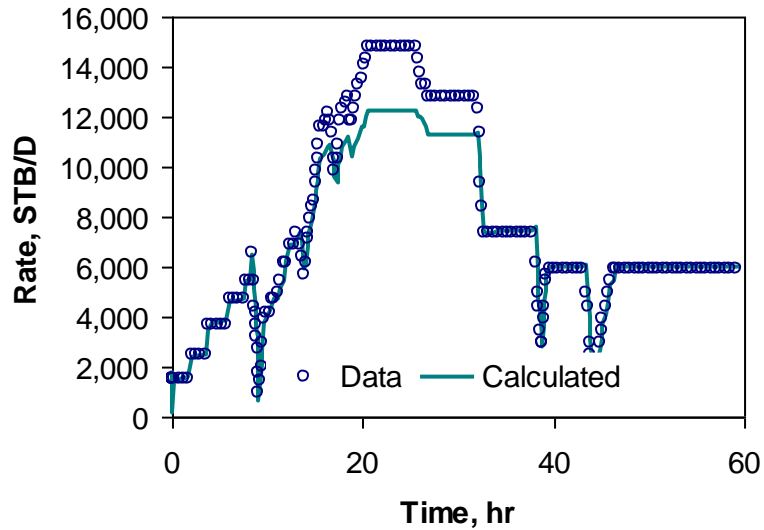**Figure 33** Matching cell temperature at 9,600 ft MD (After [48]).

Figure 34 Computed oil rate compares favorably with measured values (After [48]).

3.3 Estimating Fluid Flow Rate from Temperature Data

Kabir et al. [49] present the computational approach that estimates rates at the fluid entry point and the temperature-sensor station at a higher elevation. In this deepwater setting, temperature measurements are available during well testing up to the mudline, one every 1000 ft of TVDSS.

The authors [49] adopted a depth-dependent temperature response for a given flow rate for history matching. This modeling approach entailed the last data point from each flow period, given that the transient temperature response requires a considerable period before stabilizing. Nonetheless, the results turned out to be entirely satisfactory. Figure 35 displays the outcome of the matching history of each temperature profile, and Figure 36 shows the same outcome by cross-plotting temperature with the rate at various depths. Let us point out that only one set of input parameters helped attain this quality history match for the entire time and depth domain.
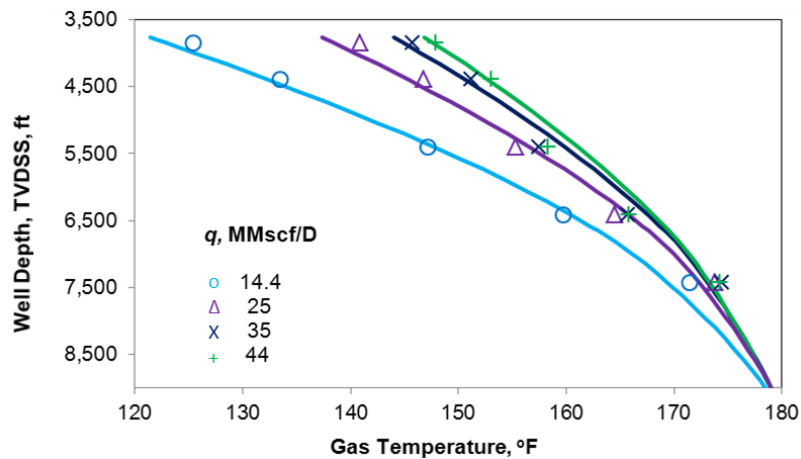

Figure 35 History matching transient temperature profiles at various rates, Well 2 (After [49]).
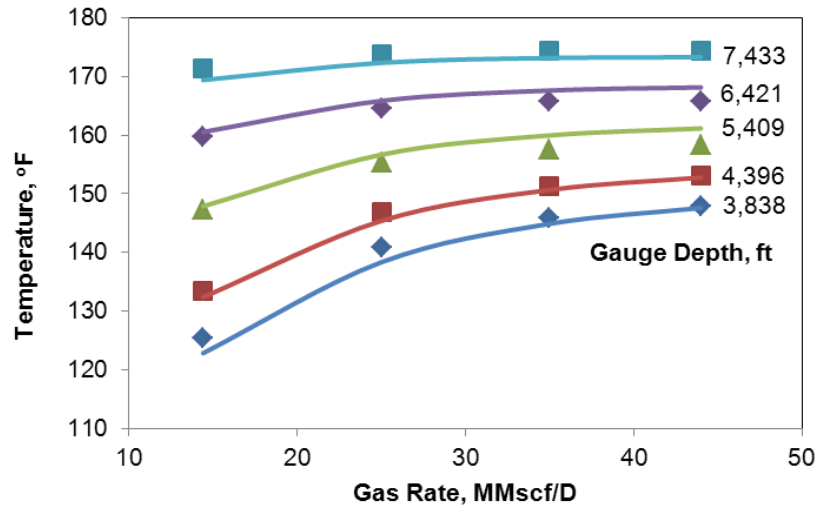
Figure 36 History matching transient temperature profiles at various rates, Well 2.

The error analysis in Table 4 shows that the solutions obtained have good accuracy at low rates but not high ones. One lesson learned here is that Joule-Thomson cooling becomes relevant with increasing rates, as Figure 37 indicates. This observation implies that the flatter temperature response induces a more significant error in the solution quality because the loss of response fidelity comes into play; Rates 3 and 4 are cases in point.

Table 4 Error estimation in computed rates, Well 2 (After [49]).

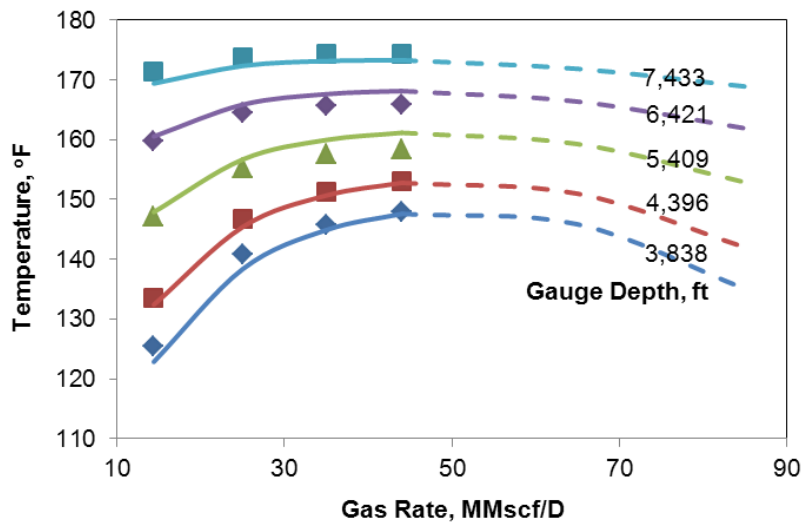|	Flow Rate, MMscf/D			
	Rate 1	Rate 2	Rate 3	Rate 4
Computed	14.9	25.0	33.2	49.7
Measured	14.40	25.02	34.95	44.00
Error, %	3.29	0.00	-5.11	12.91

Figure 37 The gas exhibits J-T cooling at higher rates, Well 2 (After [49]).

3.4 Establishing Flowing and Static Temperature Gradients

Flow rate estimation from temperature logs dates to the 1970s; the Curtis and Witterholt [50] in producing wells and Witterholt and Tixier [51] studies in injection wells provide the relevant outcomes. Similarly, the heat-transfer model provides the temperature response related to fluid influx along the wellbore in production logging, leading to zonal contributions ascertained with a heat-transfer model. Subsequent studies of Wang et al. [52], Kabir et al. [49], and Al Saedi et al. [53] are cases in point.

Although geothermal gradient is crucial to many engineering analyses, systematic methods are lacking in the industry. Formation testers and drill-stem tests provide the necessary data when transient tests when several depth intervals are involved. The use of openhole logs requires multiple passes to collect time-dependent temperature data for extrapolation. This section illustrates the use of distributed temperature sensors in estimating static and dynamic temperature gradients.

Figure 38 presents the flowing temperature gradients for four producers completed at different depths. This figure points out that the source of reservoir energy associated with depth governs the outcome of the flowing temperature gradient; Well 3's significant rate advantage (68 MMscf/D) over other wells does not change the outcome of a higher energy source for Well 4. The opposite outcome becomes true for Wells 1 and 2, which experience lower energy sources. The lesson learned here is that the flowing temperature gradient is unique to the reservoir of interest. This information is crucial to casing design for mitigating the annular-pressure buildup (APB) in the B- and C-annuli at the top of cement in subsea completions. In other words, thicker pipes, vacuum-insulated tubing, syntactic foam, and burst and collapse disks come into play in high-temperature system designs.
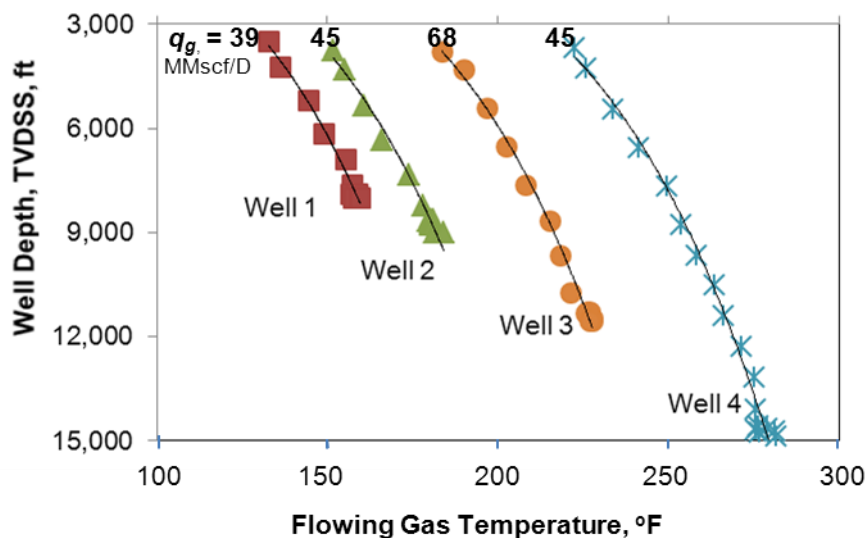

Figure 38 Flowing temperature gradients tied uniquely to the energy source or reservoir depth (After [49]).

Let us discuss how the information gathered during pressure-transient testing provided the necessary platform to establish the static geothermal gradient in this deepwater system. For Well-2, a nearly 100-hr shut-in period during the last buildup provided an opportunity to obtain the static-formation temperature (T_{ei}) at each depth. Figure 39 displays the temperature falloff response on

the diagnostic log-log plot at three depths. The lower curve associated with each depth represents the derivative signature, which shows near-stabilization of the plateau, suggesting the infinite-acting period. We can then curve-fit this infinite-acting data and beyond with the rectangular-hyperbola approach to estimate the formation temperature, T_{ei}. Figure 40 typifies the fit quality with the rectangular-hyperbola approach at a given depth.
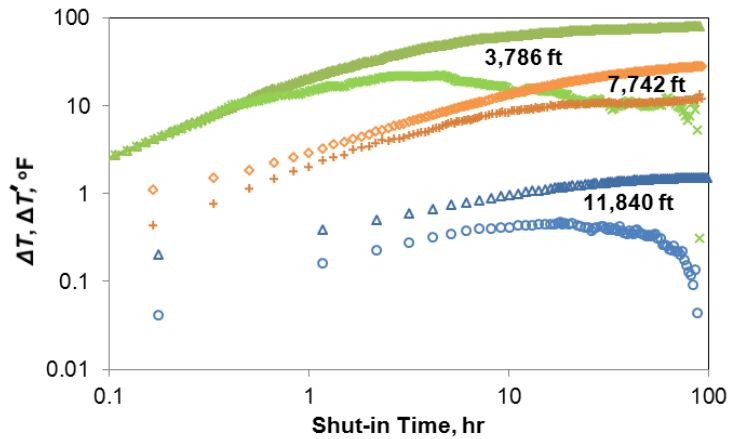

Figure 39 Log-log signatures of temperature decay during well shut-in at various depths, Well 2 (After [49]).
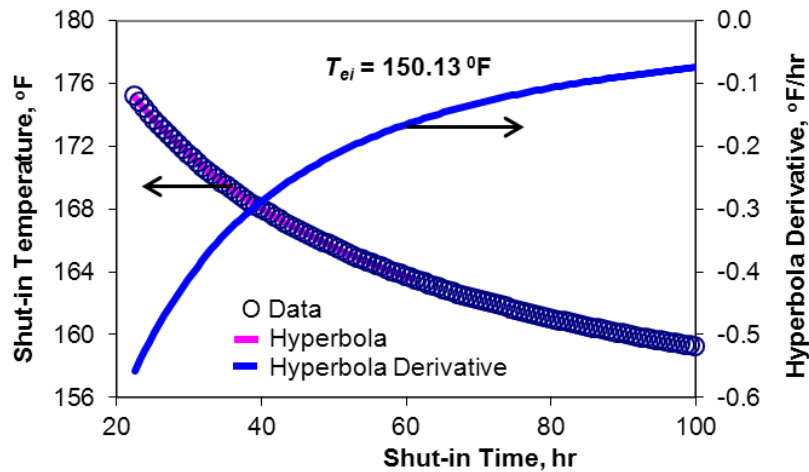

Figure 40 Estimating formation temperature @7,742 ft with rectangular-hyperbola analysis, Well 2 (After [49]).

Following this approach of temperature falloff analysis of all four wells at various depths, we observed two static-gradient signatures, as Figure 41 displays. These two static gradients are 0.0247°F/ft for the shallower horizon and 0.015°F/ft for the deeper horizon. The change in the two gradients occurs at a depth of about 9,200 ft, which is stratigraphic Jurassic/Triassic. Let us point out that the temperature-derivatives at two depths, 3,786 and 7,742 ft, overlay, thereby suggesting the same rock conductivity, whereas that at 11,840 ft, is shallower, suggesting higher rock conductivity, as indicated by a steeper geothermal gradient. This analysis appears very holistic, given that the temperature sensors in openhole logs do not have the necessary residence time nor the resolution to estimate the static temperature accurately.
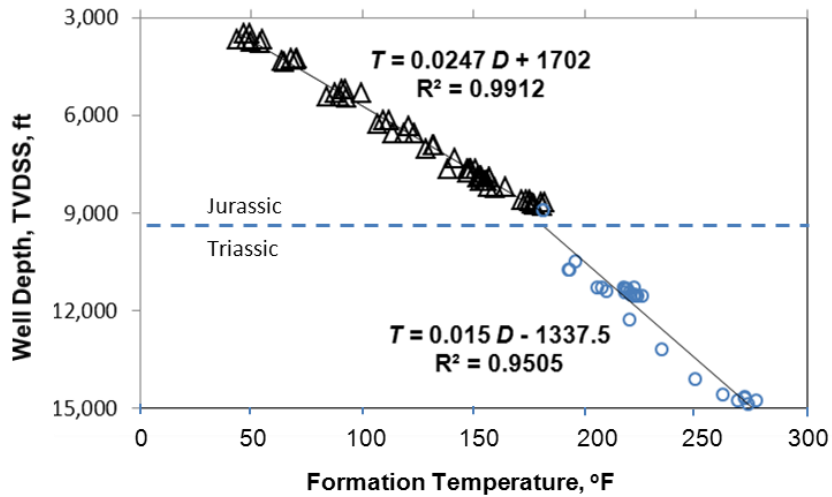
Figure 41 Estimating geothermal gradient with estimated formation temperatures at various depths (After [49]).

In a follow-up study, Al Saedi et al. [53] offered a new methodology for estimating the geothermal gradient from three shut-in tests. They showed that invoking the superposition principle could establish a reliable geothermal gradient. Figure 42 displays temperature and flow rate profiles and contains three shut-in periods in this transient test sequence. The temperature profiles during these shut-in periods appear in Figure 43. The authors [53] demonstrated that the second and third shut-in period profiles could align by applying the superposition principle, as Figure 44 exhibits.
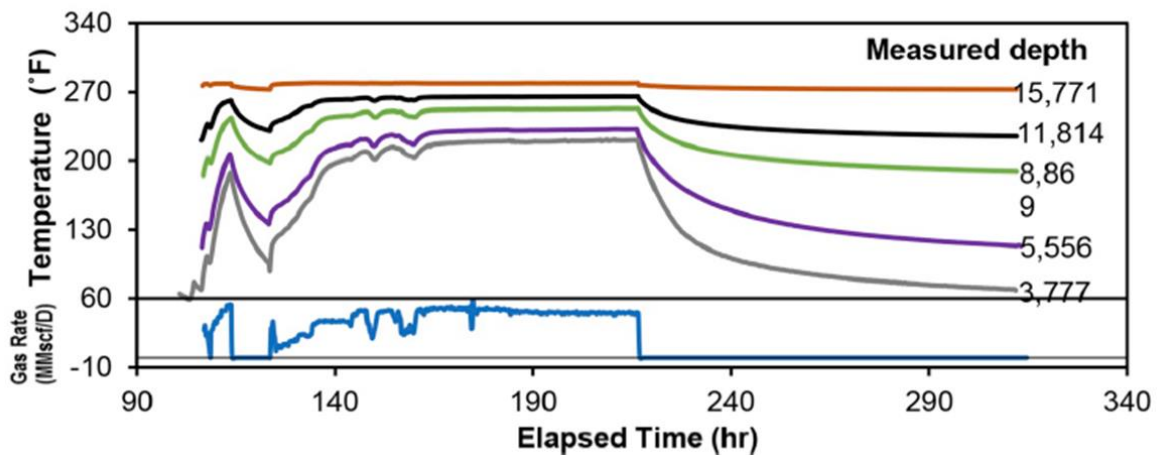

Figure 42 Depth-dependent measurements of transient temperature in Well 4 (After [53]).
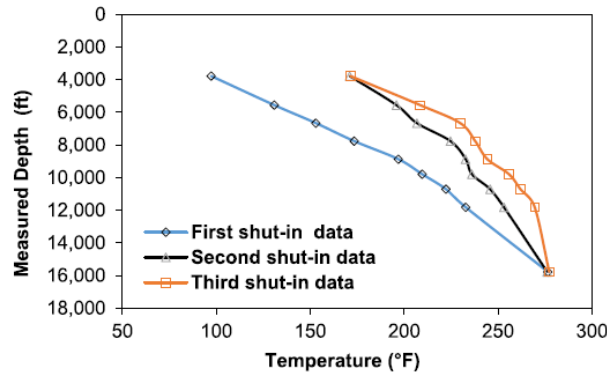
Figure 43 Estimated formation temperature for three shut-in periods (After [53]).
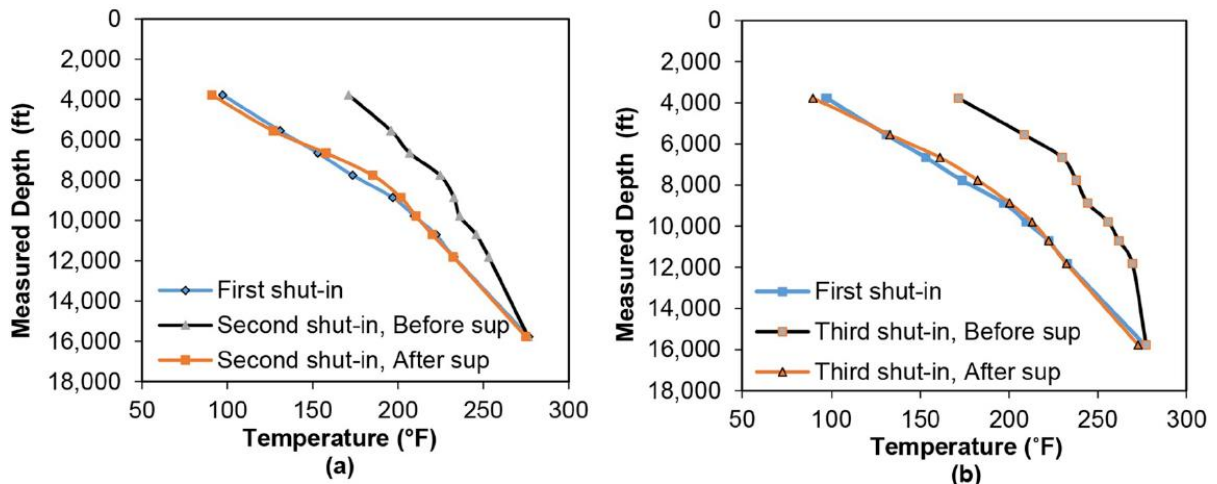

Figure 44 Wellbore temperature profiles without and with superposition: 2nd shut-in (a), 3rd shut-in (b). (After [53]).

3.5 Heat-Flow Rate Estimation from Fluid-Flow Rate & Related Applications

Many investigations have appeared in the literature on transient-temperature analysis in hydrocarbon and geothermal reservoirs. Some of these studies include those of App and Yoshioka [54], Duru and Horne [55], Mao and Zeidouni [56, 57], Onur et al. [58], Galvao et al. [59], and Al Saedi and Kabir [60-62], among others. Besides estimating the initial formation temperature, handling the gauge placement and Joule-Thompson or J-T effect became the focal points of some of these studies.

Here, we focus on estimating the heat-flow rate from the fluid-flow rate to facilitate the superposition approach for the initial-formation temperature estimation, analogous to that in pressure-transient analysis. The methodology and solution approach appears in [60, 61]. Let us start with the wells discussed in Section 3.4 to illustrate how a multirate test can unveil the static formation temperature or T_{ei}. Figure 45 presents the temperature measurements at two depths in a deepwater gas well, as elaborated in [61]. Although stable temperatures appear up to 96 hours, they do not necessarily represent the actual formation temperature given the scale here.
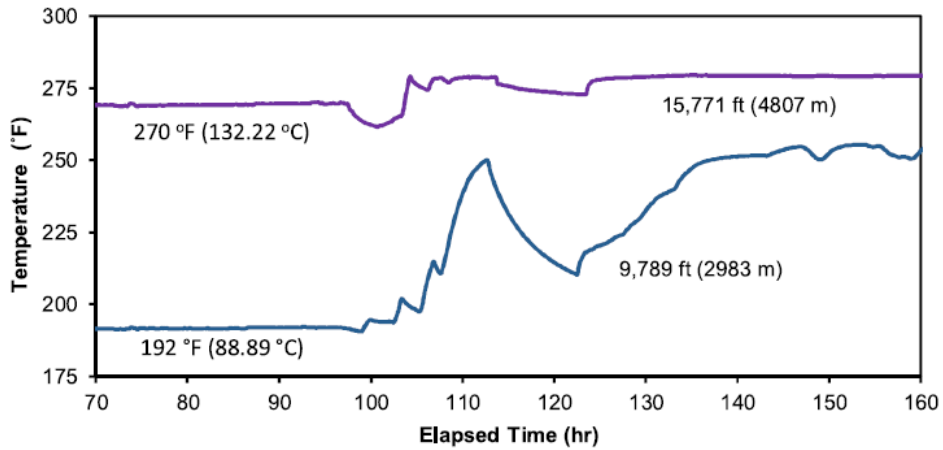
Figure 45 Measured formation temperature for the second shut-in period at two depths (After [60]).

Figure 46 suggests that the lower derivative plateau at the deeper interval signifies that the formation has much higher thermal conductivity than the shallower depth. This observation explains why we have two different geothermal gradients, as shown in Figure 41. The heat flow rate trajectory in Figure 46b also indicates that the lower-conductive shallower formation will take much longer to equilibrate when a shut-in period occurs relative to the deeper interval.
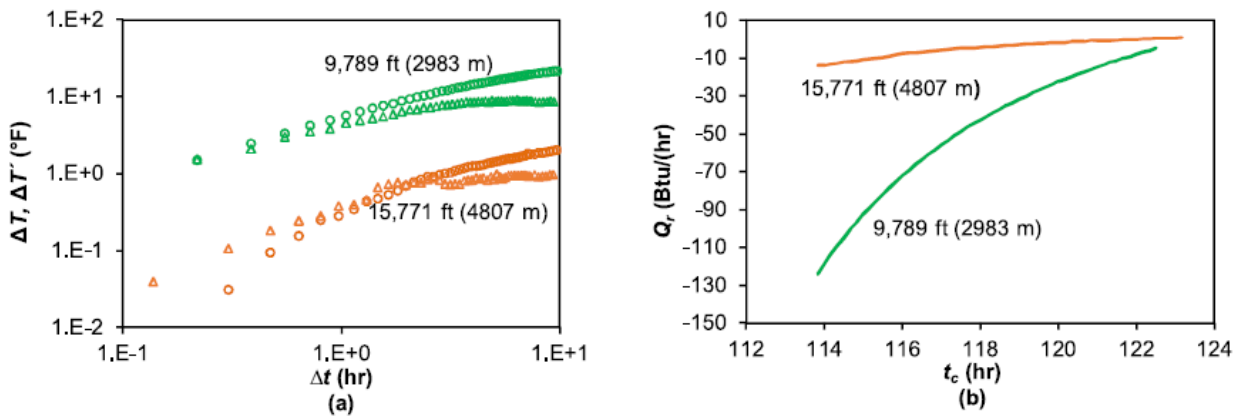
Figure 46 Temperature buildup response suggests a long thermal storage period (a), estimated heat flow rate (b) (After [60]).

Let us discuss how the temperature works when the principle of superposition is enacted. Figure 47a and Figure 48a show the heat flow direction results during the well shut-in periods. This flow direction dictates which way the superposition straight line evolves. At the shallower depth of 2983 m, the heat flow occurs from the wellbore to the adjacent formation due to the production-induced higher wellbore temperature than the formation. However, at the deeper depth of 4807 m, the heat flow occurred from the formation into the wellbore, as the flipping of the plotting variables in Figure 48a displays.

Figure 47 Temperature behavior at 2983 m; superposition response (a), static-formation temperature from the regressed line (b) (After [60]).
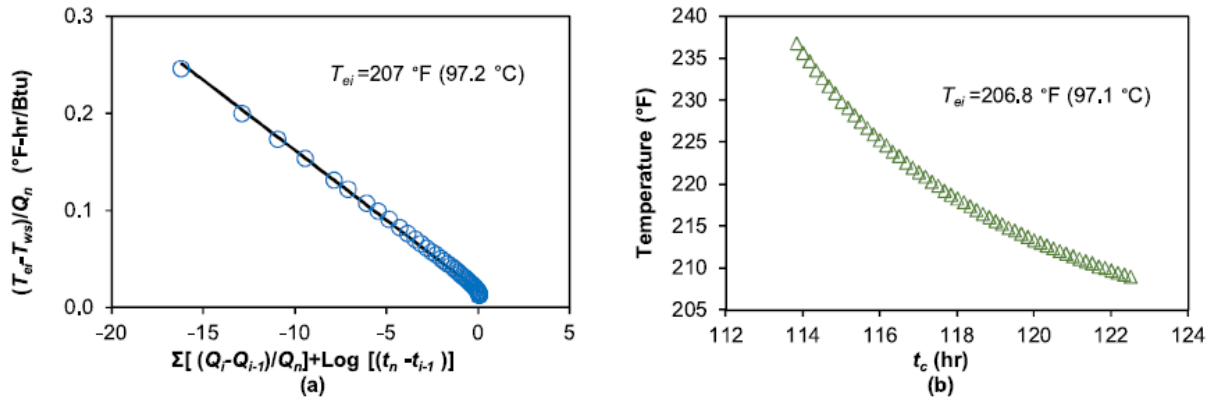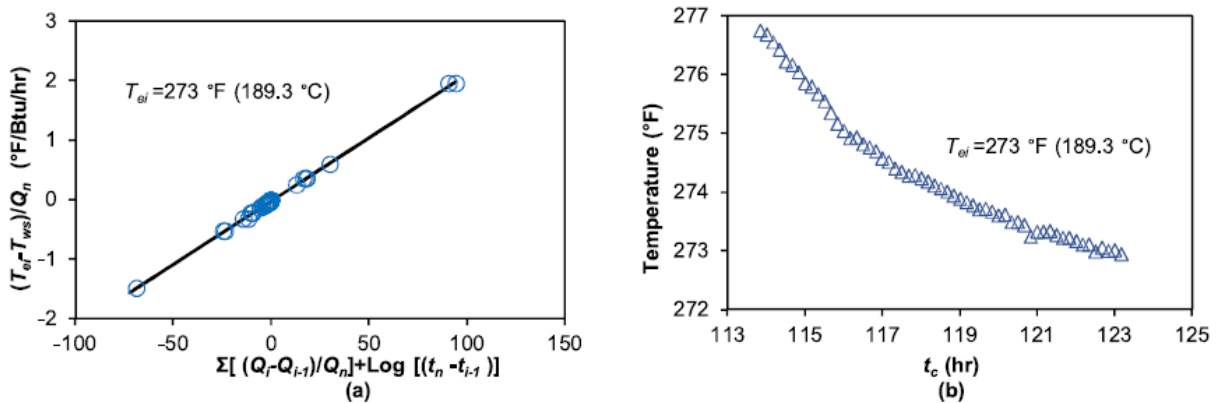

Figure 48 Temperature behavior at 4807 m; superposition response (a), static-formation temperature from the regressed line (b) (After [60]).

Another related study [61] showed that estimating the initial-formation temperature (T_{ei}) from the fluid-flow rate and the associated thermal radius of about 0.41 ft from the wellbore is feasible. This computational approach provides a more stable initial formation temperature estimation, given that the heat transfer rate is intrinsically low. Convective heat transfer appeared to be the predominant heat-transfer mechanism. This heat-flow model can handle both increasing and decreasing rate sequences, meaning its use in various realistic field settings is feasible, and the Joule-Thompson effect is implicit in its formulation. The convolution approach also offers another way of estimating the static-formation temperature. Figure 49 presents the field data for this oil well; Figure 50a shows the oil and the associated heat flow rates, and Figure 50b displays the evolution of the T_{ei} profile.
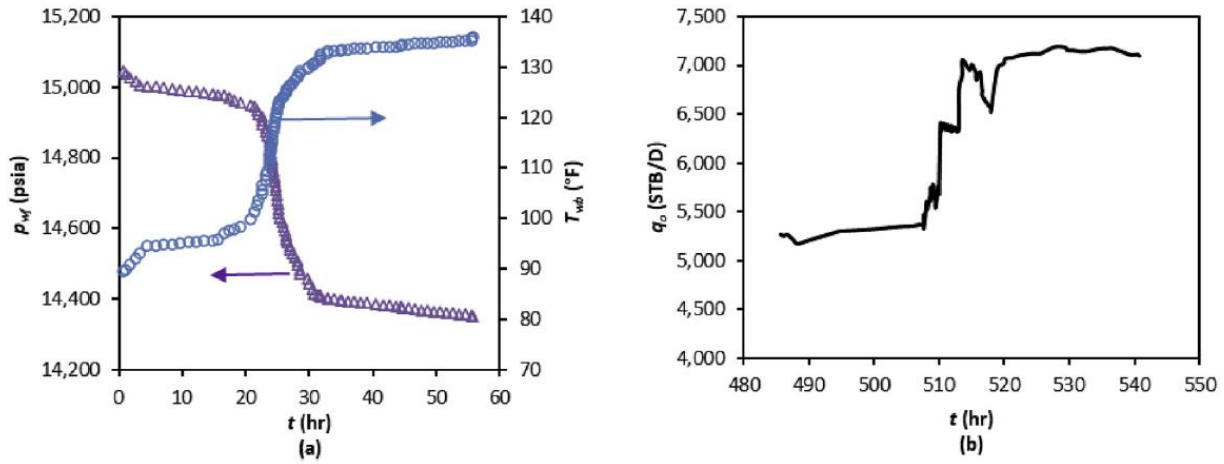
Figure 49 Field dataset containing downhole pressure and temperature (a), and oil flow rate (b) (After [61]).
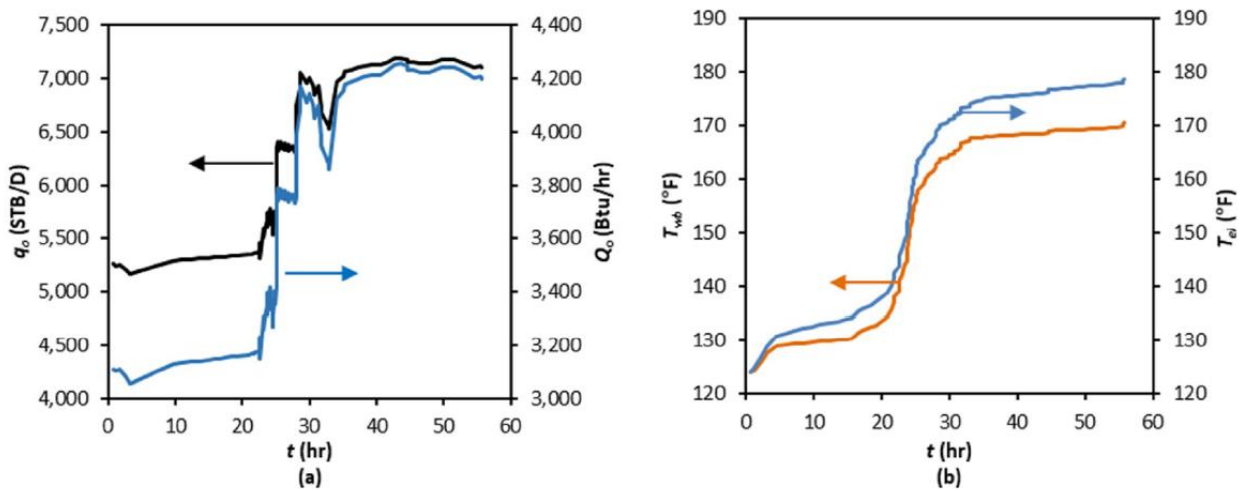
Figure 50 Results corresponding to fluid flow; Heat flow rate (a), Static formation temperature (b) (After [61]).

In summary, evaluating the heat-flow rate and static-formation temperature becomes feasible even when multiple sequential fluid-flow rates lead to a corresponding change in heat-flow rates from or to the wellbore. Consequently, the rate-convolution approach works quite well, given the pressure and temperature-diffusivity equations analogy. Even ±25% uncertainty in the diffusivity constant α results in a T_{ei} error of less than 2.5%. Using the temperature-derivative plateau as a guide can considerably enhance the solution quality, given that the early-time storage period can disappear for any analysis. Besides, the convolution of temperature with the heat-flow rate can lead to quality solutions for T_{ei} in a shut-in period.

3.6 Fluid Circulation in Wellbores for Drilling and Energy Extraction

3.6.1 Fluid Temperature Modeling in Drilling Operations

The energy balance equation in a vertical wellbore leads to a second-order differential equation,

which translates into a boundary-value problem. Applying the boundary conditions or B.C. led to the revealing of two unknown constants. Historically, investigations had been limited to using the first kind of B.C. or Dirichlet condition. The study of Al Saedi et al. [62] introduced two other B.C.s; the second kind, or the Neumann condition, and the third kind, or the Robin condition. For clarity, they named these models in a sequence of BCs as Model-1, Model-2, and Model-3, as Figure 51 depicts in sequence.
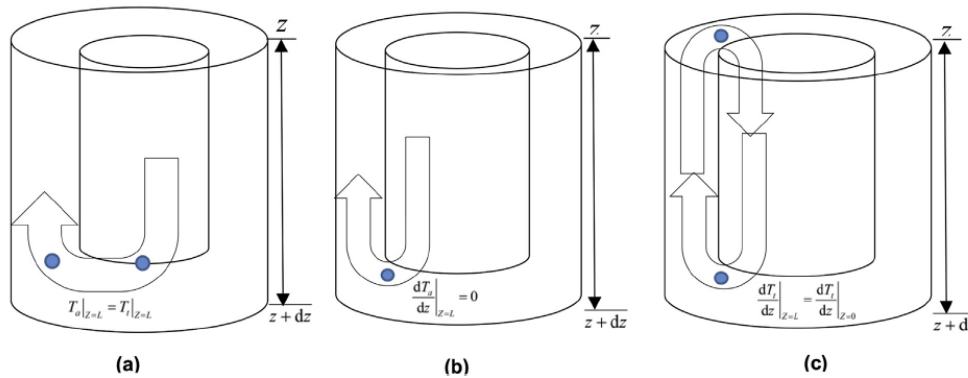

Figure 51 Three boundary conditions: (a) Dirichlet, (b) Neumann, (c) Robin (After [62]).

The application of Model-2 and Model-3 will result in different temperature profiles due to changes in the B.C.s. The annular temperature is higher due to the heat gain from the formation than the drill-pipe temperature profile for the forward circulation. But the opposite happens for the reverse circulation case. Figure 52 presents the results of all three models for the forward and reverse-circulation cases. In both situations, the use of Model-2 and Model-3 indicates an increase in temperature profiles, leading to higher bottomhole temperatures. In a drilling operation, this increase in temperature can be justified by the frictional energy and the rotational and drag forces.

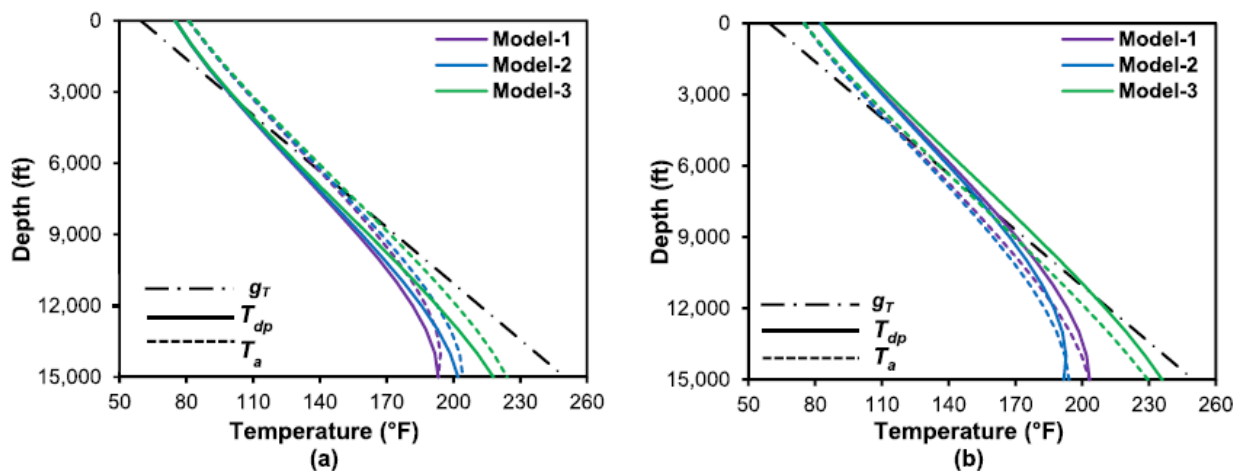**Figure 52** Results of three models: forward circulation (a), reverse circulation (b) (After [62]).

Despite the long drilling history in the U.S. that started in the 1920s, the fluid circulation modeling with increasing depth became necessary with increased formation temperature for managing the mud density and viscosity for the cutting transport from downhole to surface. Although early fluid

circulation models appeared in the 1960s [63, 64], their practical applications became a challenge, given the required information they needed. Recently, the article of Al Saedi et al. [62] offered simplified models with three independent boundary conditions to handle increased temperature settings.

Subsequently, the same authors [65] proposed physics-based models involving frictional (FE) or rotational kinetic energy (RKE) that represent the mechanical aspects of the drill-bit operation. As Al Saedi et al. [65] detailed, the drilling process in a deviated well provides a contact area of the drill string with the wellbore. This reality may affect the overall heat-transfer coefficient from the annulus to the drillpipe, *U*. However, the overall heat-transfer coefficient from the formation to the annulus remains constant with the steady-state assumption. Therefore, by retaining the same data and changing *U* for each stand, one can get a good match with the measured data for MWD1 and MWD2. As Figure 53 shows, invoking the RKE model raised the temperature by about 15°F.

Figure 53 Adding RKE to annulus vs. measured data by changing overall heat-transfer coefficient, MWD1 (a), MWD2 (b) (After [65]).

Let us note that the wellbore does not have uniformity in a deviated drilling operation, even for an inclination of about 10° in the tangent section. Therefore, the heat generated by frictional energy arising from the physical contact of the drill string with the wellbore wall is unlikely to occur uniformly in the entire wellbore. In contrast, the application of RKE depends on the rotational speed of the drill string regardless of its contact with the wellbore, as described earlier by Kumar and Samuel [66]. As a result, the temperature profiles from the RKE will be higher than those obtained by the FE model.

Subsequently, Al Saedi et al. [65] demonstrated the efficacy of the RKE model by assuming that the drillpipe takes 60% of the total generated heat and the remaining 40% goes to the bit. Keller [67] suggested this split, which Marshall and Bentsen [68] used later. This energy split further bolsters the match quality, as Figure 54 demonstrates.
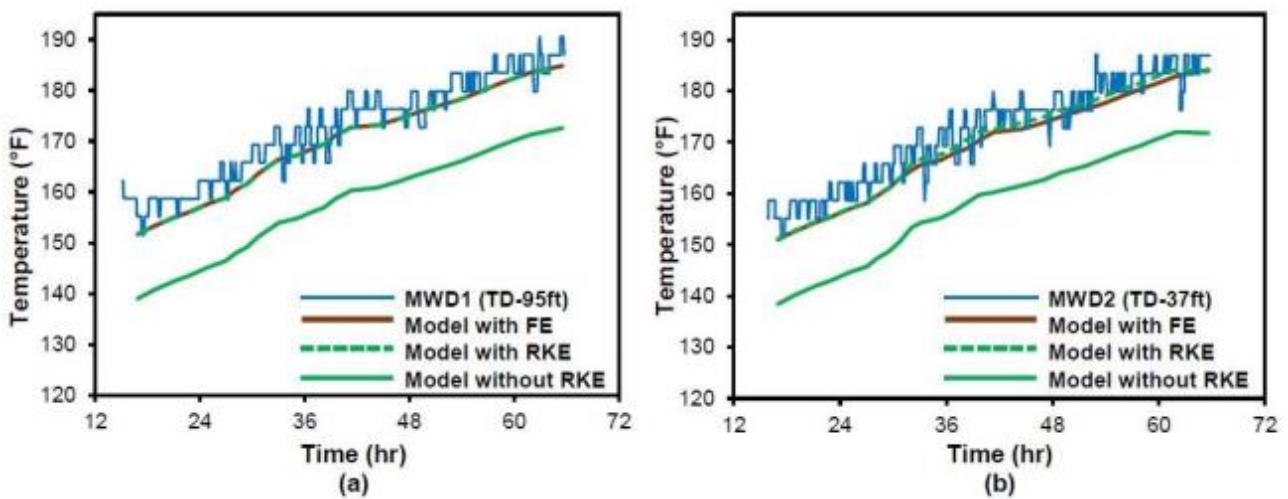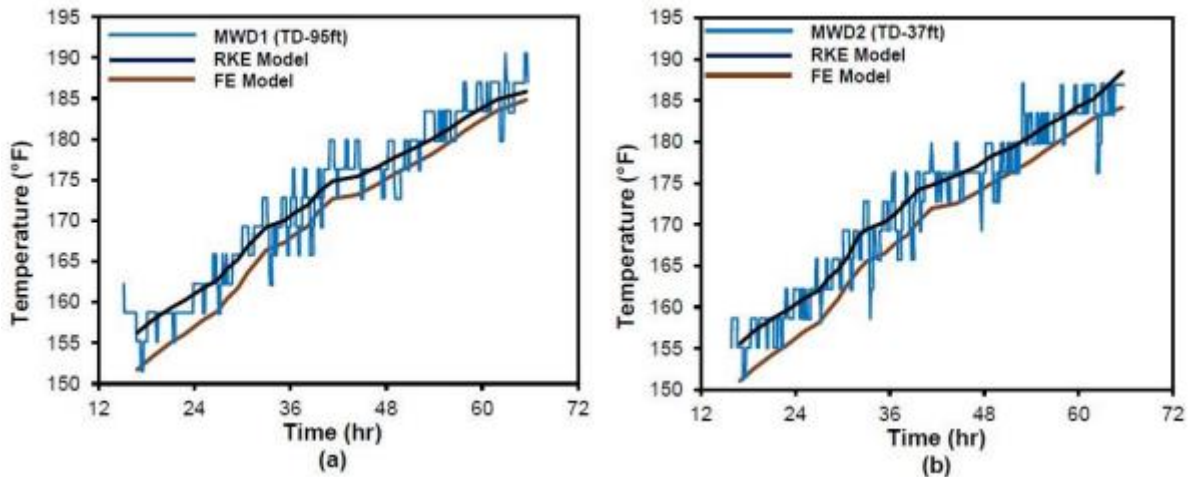
Figure 54 Adding RKE to annulus vs. measured data by changing the overall heat-transfer coefficient, MWD1 (a), MWD2 (b) (After [65]).

3.6.2 Thermal Energy Extraction by Fluid Circulation

This section explores various options for harnessing geothermal energy from a single well in various geothermal settings by circulating different fluids in a closed-loop system. To that end, a plethora of articles has appeared in the literature. The study of Hanbury and Vasquez [69] showed that geothermal energy resource offers orders of magnitude advantage over coal in terms of harmful ecological impact despite its lower thermal efficiency.

This section focuses on harnessing thermal energy by circulating a fluid in a closed-loop system, as Figure 55 displays. With an analytical approach, multiple independent variables can reveal their efficacy in supporting geothermal energy generation for various usages. Both power and hot water generation become the content of the green energy revolution that is currently underway. Note that despite very low thermal efficiency for power conversion, a meager ecological impact than coal has appeared in the recent literature [70].
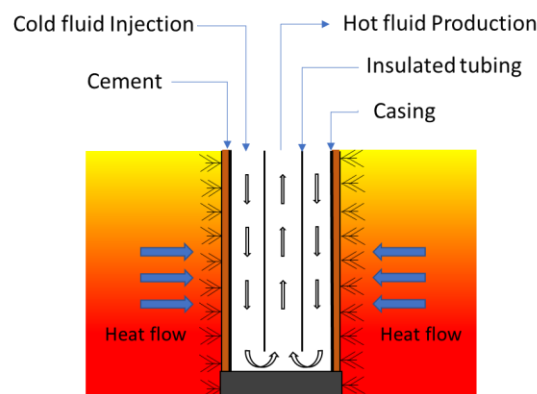
Figure 55 Schematic of the vertical wellbore heat exchanger (After [70]).

As detailed in [70], a statistical design of experiments revealed that the two most important independent variables appear to be geothermal gradient and well depth for delivering the highest fluid temperature at the wellhead. Figure 56 displays the linear relationship of these two variables with well depth. However, one key element in play pertains to the near-wellbore cooling effect due

to continuous fluid circulation, as Figure 57 shows. A subsequent study [71] revealed that a stepwise increase, followed by a stepwise decrease in circulation rate, largely mitigates this issue, as Figure 58 indicates.

Figure 56 The relationship of tubing wellhead temperature with (a) well depth and (b) geothermal gradient (After [70]).
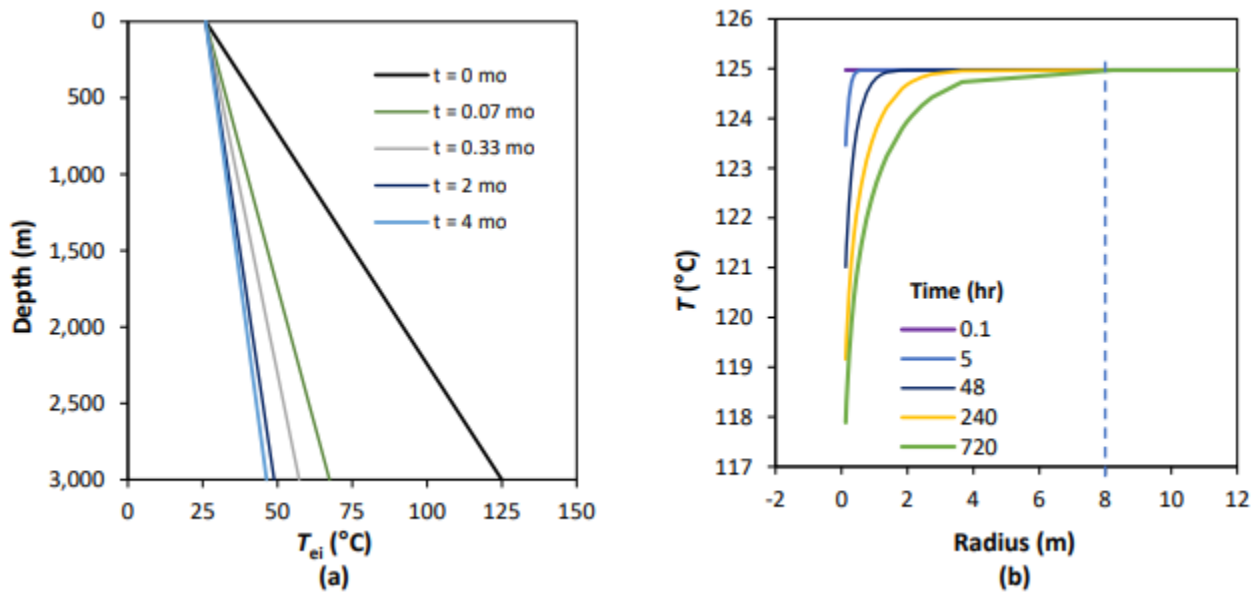
Figure 57 Variable geothermal gradient over four months of circulation (a), radial propagation of temperature transients (b) (After [71]).
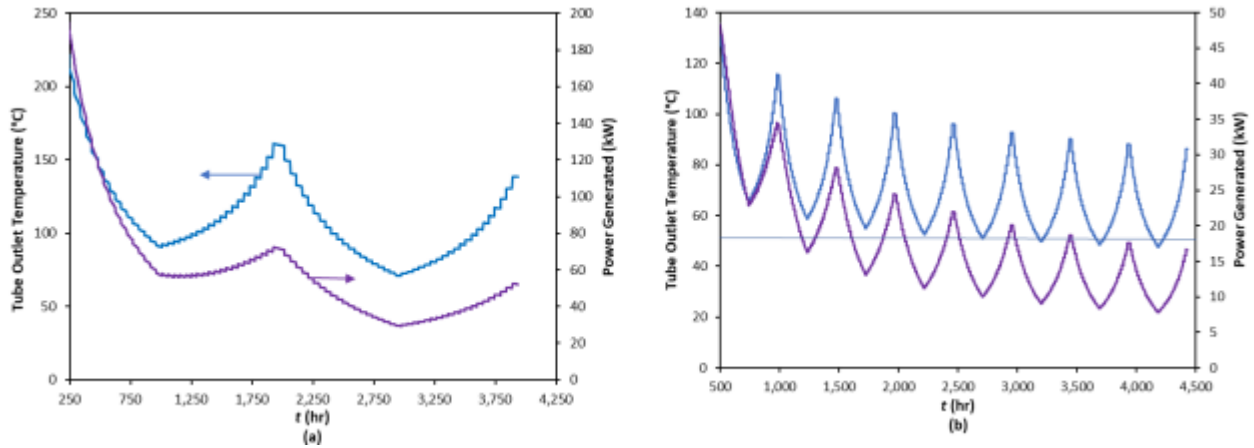
Figure 58 A high-g_T system (0.055°C/m) can produce more power (a) than the low-g_T system (0.033°C/m) despite timesteps (b) (After [71]).

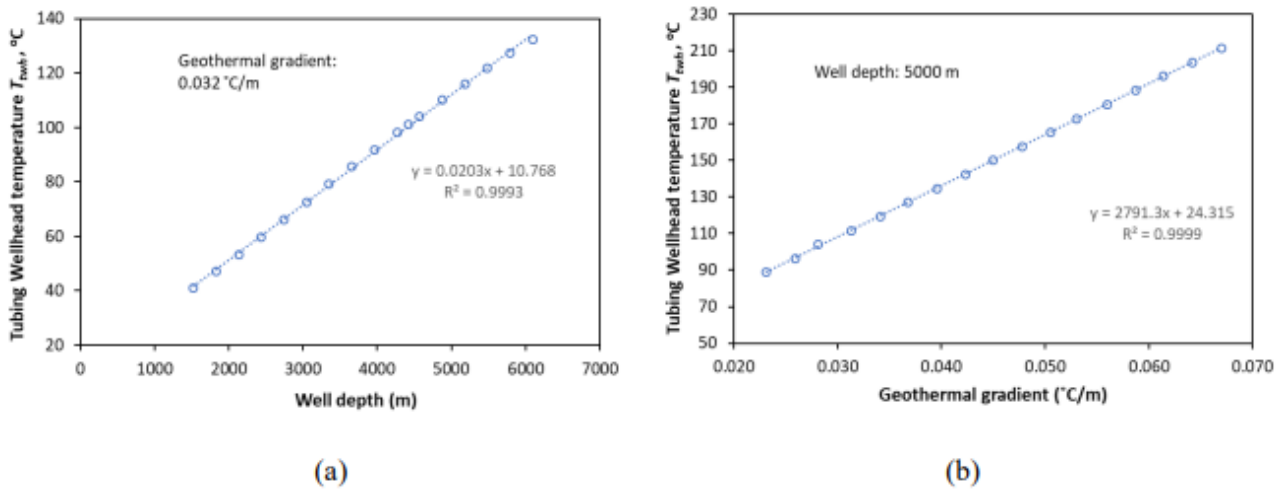After that, the study of Benavides et al. [72] showed that the day/night intermittent or periodic cycle retains a stable output temperature profile at the surface. Figure 59 demonstrates this recurring cycle's efficacy compared to the continuous and stepwise cycling strategies.
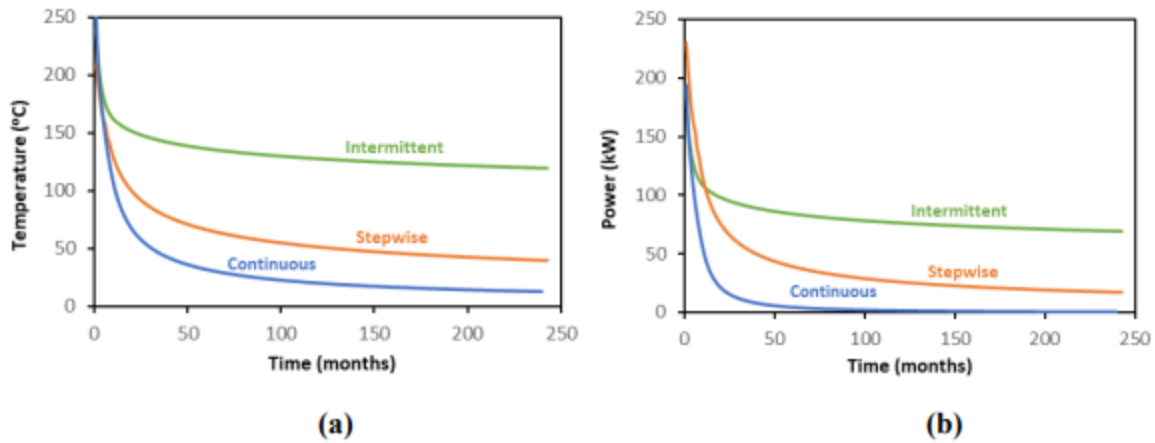
Figure 59 The intermittent cycle assures high-temperature outcome (a), and the resulting power output over 20 years (b) (After [72]).

Let us instill confidence in the outcome of these newly developed models. The circulation model's verification started with several fluids, such as water, Pentane, refrigerant R134a, and CO_2. Figure 60a shows satisfactory reproduction of the solution outcome, as reported earlier by Zhang et al. [73], except for two fluids at early times. Figure 60b, exhibiting Hu et al.'s [74] field data in Alberta, Canada, corroborates the model's validation in water circulation. The model's formulation in [72] implicitly handles two-phase flow when they experience phase change over a wide range of operating pressure and temperature in deep wells.
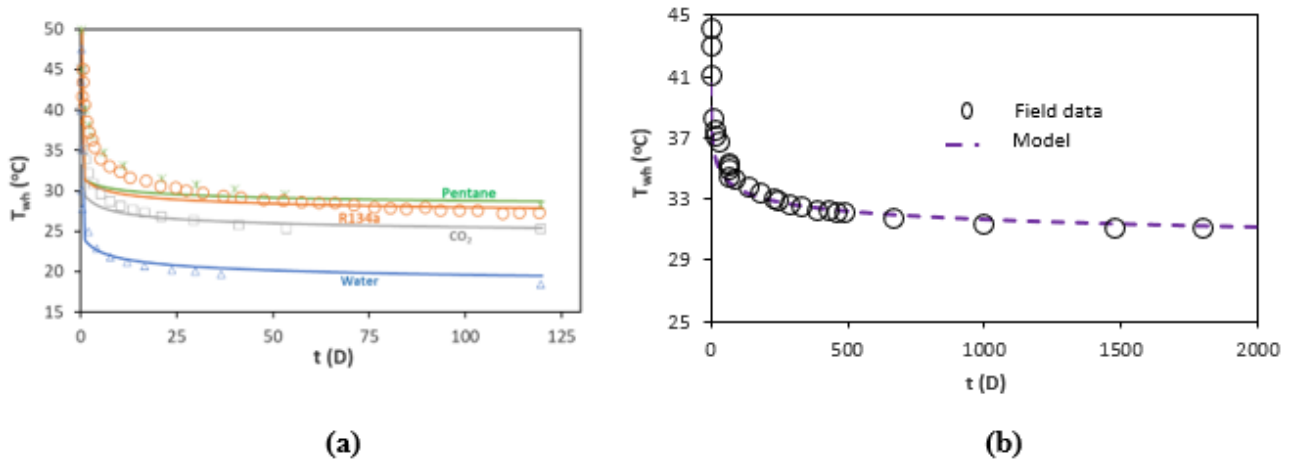
Figure 60 Gauging model performance with published data [73] for four different fluids (a); Model validation for water circulation in an Alberta field test, Hu et al. [74] (b) (After [72]).

Given Pentane's advantage over other fluids, specifically, its heat-carrying capacity, the latest study of Benavides et al. [72] contrasted the performance of Pentane and water, as Figure 61a displays. This case involved a circulation rate of 6.4 m^3/h for a geothermal gradient of 0.11°C/m in a 12-h on/off circulation cycle. The much superior performance of Pentane stems from its heat-carrying capacity due to its lower specific heat or C_p, as Figure 61b illustrates. In addition, the thermal conductivity of Pentane is about an order of magnitude lower than water; that is, 0.072 W/m-°C for pentane and about 0.67 W/m-°C for water after one year of circulation.
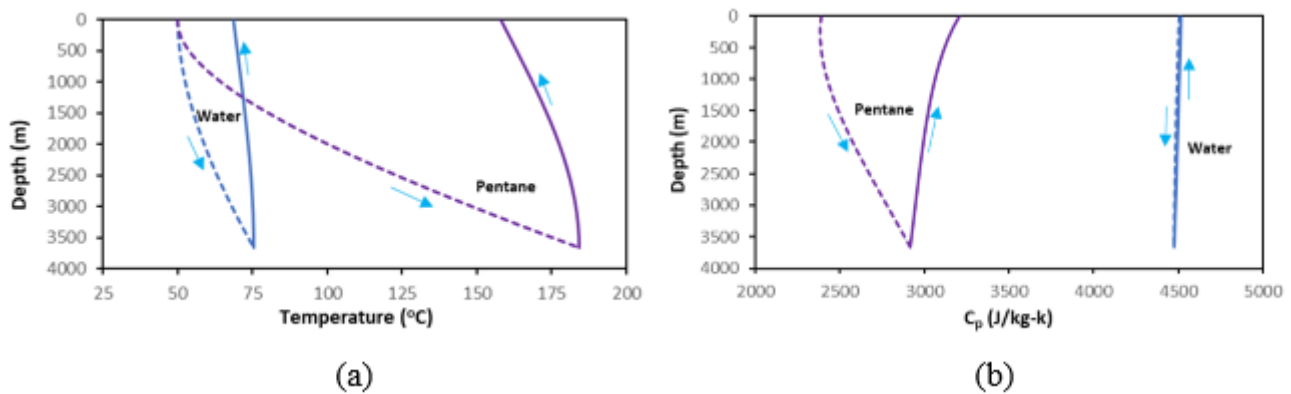
Figure 61 Wellbore fluid temperature profiles for water and pentane (a); Pentane has a superior heat-carrying capability than water (b) (After [72]).

Benavides et al. [72] used a combined approach in the intermittent cycle by adopting a hybrid strategy to show the value-added proposition at an industrial scale. This approach involved thermal/solar/wind, plus 25% from the grid in the current energy transition phase. Figures 62a and 62b initially helped us understand the economic value proposition by combining the various sources of energy and power conversion efficiency. The Net Present Value or NPV and Levelized Cost of Electricity or LCOE appeared close to these two combined resources, assuming a 12% power conversion efficiency in a binary power plant.
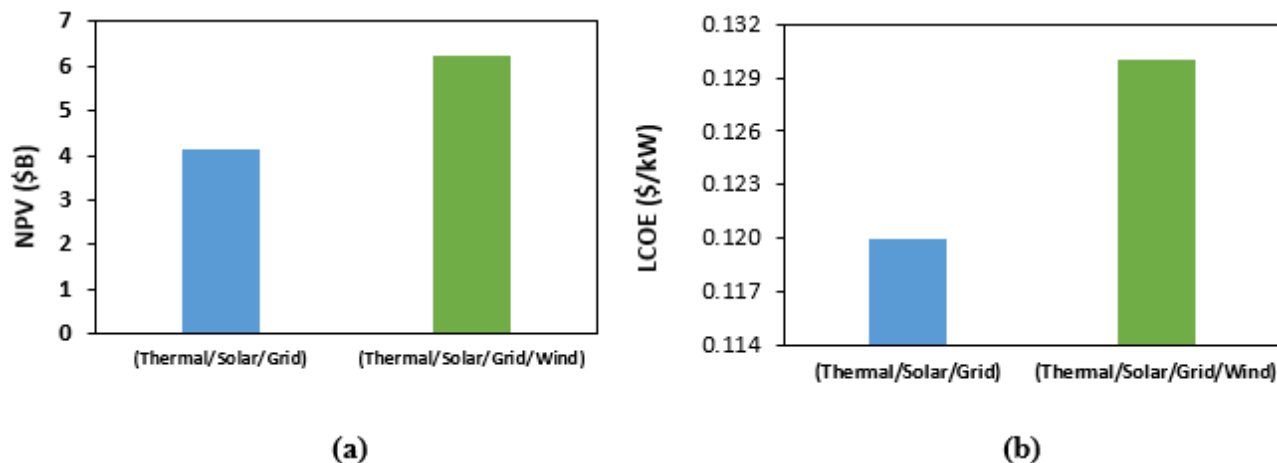
Figure 62 Relative NPV outcomes of two possible combined power sources (a); Two hybrid approaches provide reasonably close LCOE outcome (b) (After [72]).

Some of the key takeaways of this study are (a) The cyclical fluid circulation strategy involving night (thermal)/day (solar) combines the two energy sources to generate steam that leads to power generation. This approach produces a desired stable fluid temperature at the wellhead for a favorable geothermal gradient (0.11 + °C/m) and circulating fluid (e.g., pentane) are in play, (b) In low-g_T settings (0.05°C/m), the produced thermal energy generates hot water for usage in agriculture/food industries when the outlet fluid temperature ranges from 60 to 85°C.

A probabilistic approach aided objectivity for potential power generation capabilities. In addition, mingling other green energy resources, such as wind and solar, became the focal point of a hybrid strategy to minimize near-wellbore cooling associated with continuous fluid circulation.

4. Summary

Studies on multiphase fluid and heat flows in wellbores have spanned over decades. This article attempts to encapsulate some of them in reservoir fluid production and injection and some aspects of drilling and fluid-circulation operations.

Although not discussed in detail, comparative studies of two-phase flow models have shown that the performance of various mechanistic models appears similar in a statistical sense, thereby implying that perhaps the improvement in two-phase flow modeling has reached a terminal point. Instead of model improvement, the quality of input data appears to be the logical focal point in industrial applications. For example, besides oil, the fluids of lesser importance, such as gas and water, deserve equal significance in rate metering. Perhaps, the current practice of production rate validation through real-time integrated asset modeling appears very prudent. In addition, changes in oil PVT properties need attention with reservoir depletion, particularly in thick oil columns, where compositional gradient prevails.

Also, analytical models can estimate the injection profile in a stratified reservoir involving short injection and shut-in periods to assess injection conformance before starting any secondary or tertiary recovery project. The models of Hashish and Zeidouni [75, 76] are a case in point.

This article handled the management of direct implications to some of the oil industry operations but not all. Topics, including cyclic production with artificial-lift methods like gas and plunger-lift (Hashmi et al. [77], Xiang and Kabir [78]), are cases in point. Similarly, items related to fluid PVT

properties promoting solid depositions, such as asphaltene [79-82], wax [83, 84], gas hydrates [84], as addressed holistically by Pickarts et al. [85] deserve close attention before their onset. These items need handling with care by managing wellbore pressure throughout the tubing string. In addition, changes in tubular ID due to corrosion or solids buildup may adversely affect the wellbore thermal modeling, not to mention well performance.

Besides these challenges in the oil and gas industry, managing toxic items such as carbon dioxide, hydrogen sulfide, and mercury in the geothermal sector need due attention. To that end, a life-cycle analysis of geothermal power plants by Parisi et al. [86] in this sector, and wellbore corrosion, as discussed by Nogara and Zarrouk [87, 88], is noteworthy.

Acknowledgments

Author Contributions

The author did all the research work of this study.

Funding

Competing Interests

The author has declared that no competing interest exists.

References

1. Collier JG. *Convective boiling and condensation*, 2nd Ed. 1972. McGraw-Hill, New York.
2. Taitel Y, Barnea D, Dukler AE. Modeling flow pattern transition for steady upward gas-liquid flow in vertical tubes. AIChE J. 1980; 26: 345-354.
3. Hasan AR, Kabir CS. Fluid flow and heat transfer in wellbores. Richardson, Texas: Society of Petroleum Engineers; 2018.
4. Gomez LE, Shoham O, Schmidt Z, Chokshi RN, Northug T. Unified mechanistic model for steady-state two-phase flow: Horizontal to vertical upward flow. SPE J. 2000; 5: 339-350.
5. Kaya AS, Sarica C, Brill JP. Mechanistic modeling of two-phase flow in deviated wells. SPE Prod Oper. 2001; 16: 156-165.
6. Ansari AM, Sylvester ND, Sarica C, Shoham O, Brill JP. A comprehensive mechanistic model for upward two-phase flow in wellbores. SPE Prod Oper. 1994; 9: 143-151.
7. Hasan AR, Kabir CS. A simple model for annular two-phase flow in wellbores. SPE Prod Oper. 2007; 22: 168-175.
8. Pucknell JK, Mason JN, Vervest EG. An evaluation of recent "mechanistic" models of multiphase flow for predicting pressure drops in oil and gas wells. Aberdeen, Scotland: SPE Offshore Europe; 1993.
9. Kabir CS, Hasan AR. Performance of a two-phase gas/liquid flow model in vertical wells. J Pet Sci Eng. 1990; 4: 273-289.

10. Hagedorn AR, Brown KE. Experimental study of pressure gradients occurring during continuous two-phase flow in small-diameter vertical conduits. J Pet Tech. 1965; 17: 475-484.

11. Bendlksen KH, Malnes D, Moe R, Nuland S. The dynamic two-fluid model OLGA: Theory and application. SPE Prod Eng. 1991; 6: 171-180.

12. Hasan AR, Kabir CS, Sayarpour M. Simplified two-phase flow modeling in wellbores. J Pet Sci Eng. 2010; 72: 42-49.

13. Kabir CS, Hasan AR. Simplified wellbore-flow modeling in gas/condensate systems. SPE Prod Oper. 2006; 21: 89-97

14. Gray HE. Vertical flow correlation in gas wells. 2nd ed. In: User's manual for API 14B surface controlled subsurface safety valve sizing computer program. Dallas: American Petroleum Institute; 1978.

15. Riza MF, Hasan AR, Kabir CS. A pragmatic approach to understanding liquid loading in gas wells. SPE Prod Oper. 2015; 31: 185-196.

16. Coleman SB, Clay HB, McCurdy DG, Norris III LH. A new look at predicting gas-well load-up. J Pet Techol. 1991; 43: 329-333.

17. Veeken K, Hu B, Schiferli W. Gas-well liquid-loading-field-data analysis and multiphase-flow modeling. SPE Prod Oper. 2010; 25: 275-284.

18. Turner RG, Hubbard MG, Dukler AE. Analysis and prediction of minimum flow rate for the continuous removal of liquids from gas wells. J Pet Technol. 1969; 21: 1475-1482.

19. Chierici GL, Giannone G, Schlocchi G. A wellbore model for two-phase flow in geothermal reservoirs. In: SPE annual technical conference and exhibition. San Antonio: OnePetro; 1981.

20. Ambastha AK, Gudmundsson JS. Pressure profiles in two-phase geothermal wells: Comparison of field data and model calculations. Stanford, CA: Petroleum Engineering Department, Stanford University; 1986.

21. Chadha PK, Malin MR, Palacio-Perez A. Modelling of two-phase flow inside geothermal wells. Appl Math Model. 1993; 17: 236-245.

22. Garg SK, Pritchett JW, Alexander JH. A new liquid hold-up correlation for geothermal wells. Geothermics. 2004; 33: 795-817.

23. Duns Jr H, Ros NC. Vertical flow of gas and liquid mixtures in wells. Paper presented at the 6th World Petroleum Congress. 1963 June 19-26; Frankfurt am Main, Germany. Document ID: WPC-10132.

24. Hughmark GA. Pressure drop in horizontal and vertical gas liquid flow. Ind Eng Chem Fundam. 1963; 2: 315-320.

25. Ramey Jr HJ. Wellbore heat transmission. J Pet Technol. 1962; 14: 427-435.

26. Hasan AR, Kabir CS. Modeling two-phase fluid and heat flows in geothermal wells. J Pet Sci Eng. 2010; 71: 77-86.

27. Tonkin RA, O'Sullivan MJ, O'Sullivan JP. A review of mathematical models in geothermal wells. Geothermics. 2021; 97: 102255.

28. Battistelli A, Finsterle S, Marcolini M, Pan L. Modeling of coupled well-reservoir flow in steam-like supercritical geothermal systems. Geothermics. 2020; 86: 101793.

29. Zamshid-Nezhad M. Steam alternating non-condensable gas injection for more heavy oil recovery. Energy. 2022; 240: 122476.

30. Satter A. Heat losses during flow of steam down a wellbore. J Pet Technol. 1965; 17: 845-851.

31. Willhite GP. Over-all heat transfer coefficients in steam and hot water injection wells. J Pet

Technol. 1967; 19: 607-615.

32. Pacheco EF, Farouq Ali SM. Wellbore heat losses and pressure drop in steam injection. J Pet Technol. 1972; 24: 139-144.

33. Farouq Ali SM. A comprehensive wellbore steam/water flow model for steam injection and geothermal applications. SPE J. 1981; 21: 527-534.

34. Fontanilla JP, Aziz K. Prediction of bottom-hole conditions for wet steam injection wells. J Can Pet Technol. 1982; 21: PETSOC-82-02-04.

35. Zargar Z, Farouq Ali SM. Analytical treatment of steam-assisted gravity drainage: Old and new. SPE J. 2018; 23: 117-127.

36. Zargar Z, Farouq Ali SM. Effect of confinement and well interference on SAGD performance: An analytical assessment. SPE J. 2019; 24: 1595-1612.

37. You J, Rahnema H. Numerical modeling of multiphase steam flow in wellbore. J Pet Sci Eng. 2018; 164: 259-277.

38. Bahonar M, Azaiez J, Chen Z. A semi-unsteady-state wellbore steam/water flow model for prediction of sandface condition in steam injection wells. J Can Pet Technol. 2010; 49: 13-21.

39. Zhao Q, Lei Y, Zheng L Wang Y, Guo L. Numerical simulation of flow and heat transfer performance during supercritical water injection in vertical wellbore: A parameter sensitivity analysis. Int J Therm Sci. 2023; 183: 107855.

40. Ambrus A, Aarsnes UJ, Vajargah AK, Akbari B, van Oort E, Aamo OM. Real-time estimation of reservoir influx rate and pore pressure using a simplified transient two-phase flow model. J Nat Gas Sci Eng. 2016; 32: 439-452.

41. Xu Z, Song X, Li G, Wu K, Pang Z, Zhu Z. Development of a transient non-isothermal two-phase flow model for gas kick simulation in HTHP deep well drilling. Appl Therm Eng. 2018; 141: 1055-1069.

42. Liu R, Hasan AR, Mannan MS. Flow rate and total discharge estimation in gas well blowouts. J Nat Gas Sci Eng. 2015; 26: 438-445.

43. Liu R, Kabir CS, Mannan MS, Hasan AR. Estimating total discharged volume in uncontrolled oil wells. J Pet Sci Eng. 2017; 156: 373-380.

44. Oldenburg CM, Freifeld BM, Pruess K, Pan L, Finsterle S, Moridis GJ. Numerical simulations of the Macondo well blowout reveal strong control of oil flow by reservoir permeability and exsolution of gas. Proc Natl Acad Sci. 2012; 109: 20254-20259.

45. Michael A, Gupta I. Wellbore integrity after a blowout: Stress evolution within the casing-cement sheath-rock formation system. Results Geophys Sci. 2022; 12: 100045.

46. Spaulding M, Li Z, Mendelsohn D, Crowley D, French-McCay D, Bird A. Application of an integrated blowout model system, OILMAP DEEP, to the Deepwater Horizon (DWH) spill. Mar Pollut Bull. 2017; 120: 37-50.

47. Hasan AR, Kabir CS, Wang X. Wellbore two-phase flow and heat transfer during transient testing. SPE J. 1998; 3: 174-180.

48. Izgec B, Hasan AR, Lin D, Kabir CS. Flow rate estimation from wellhead pressure and temperature data. SPE Prod Oper. 2010; 25: 31-39.

49. Kabir CS, Yi X, Jakymec M, Hasan AR. Interpreting distributed-temperature measurements in deepwater gas-well testing: Estimation of static and dynamic thermal gradients, and flow rates. SPE Prod Oper. 2014; 29: 97-104.

50. Curtis MR, Witterholt EJ. Use of the temperature log for determining flow rates in flow rates in

producing wells. Paper presented at the fall meeting of the society of petroleum engineers of AIME; 1973 September 30-October 3; Las Vegas, Nevada. Richardson, Texas: OnePetro.

51. Witterholt EJ, Tixier MR. Temperature logging in injection wells. Paper presented at the fall meeting of the society of petroleum engineers of AIME; 1972 October 8-11; San Antonio, Texas. Richardson, Texas: OnePetro.

52. Wang X, Lee J, Thigpen B, Vachon GP, Poland SH, Norton D. Modeling flow profile using distributed temperature sensor DTS system. Paper presented at the intelligent energy conference and exhibition; 2008 February 25-27; Amsterdam, The Netherlands. Richardson, Texas: OnePetro.

53. Al Saedi AQ, Flori RE, Kabir CS. Estimating the initial-formation temperature and flowing-temperature gradient with transient-temperature analysis: Applications in gas reservoirs. J Nat Gas Sci Eng. 2019; 66: 126-137.

54. App J, Yoshioka K. Impact of reservoir permeability on flowing sandface temperatures: Dimensionless analysis. SPE J. 2013; 18: 685-694.

55. Duru OO, Horne RN. Simultaneous interpretation of pressure, temperature, and flow-rate data using Bayesian inversion methods. SPE Res Eval Eng. 2011; 14: 225-238.

56. Mao Y, Zeidouni M. Accounting for fluid-property variations in temperature-transient analysis. SPE J. 2018; 23: 868-884.

57. Mao Y, Zeidouni M. Dynamic temperature analysis under variable rate and pressure conditions for transient and boundary dominated flow. Trans Porous Media. 2019; 128: 45-73.

58. Onur M, Ulker G, Kocak S, Gok IM. Interpretation and analysis of transient-sandface- and wellbore-temperature data. SPE J. 2017; 22: 1156-1177.

59. Galvao MS, Carvalho MS, Barreto AB. A coupled transient wellbore/reservoir-temperature analytical model. SPE J. 2019; 24: 2335-2361.

60. Al Saedi AQ, Kabir CS. Estimation of heat-flow rate from fluid flow rate. J Pet Sci Eng. 2020; 191: 107203.

61. Al Saedi AQ, Kabir CS. Estimation of heat-flow rate: A precursor to the transient-temperature analysis. Geothermics. 2020; 83: 101732.

62. Al Saedi AQ, Flori RF, Kabir CS. New analytical solutions of wellbore fluid temperature profiles during drilling, circulating, and cementing operations. J Pet Sci Eng. 2018; 170: 206-217.

63. Edwardson MJ, Girner HM, Parkison HR, Williams CD, Matthews CS. Circulation of formation temperature disturbances caused my mud circulation. J Pet Technol. 1962; 14: 416-426.

64. Tragesser AF, Crawford PB, Crawford HR. A method for calculating circulating temperatures. J Pet Technol. 1967; 19: 1507-1512.

65. Al Saedi AQ, Flori RF, Kabir CS. Influence of frictional or rotational kinetic energy on wellbore-fluid/temperature profiles during drilling operations. SPE J. 2019; 34: 128-142.

66. Kumar A, Samuel R. Analytical model to predict the effect of pipe friction on downhole fluid temperatures. SPE Drill Complet. 2013; 28: 270-277.

67. Keller HH, Couch EJ, Berry PM. Temperature distribution in circulating mud columns. SPE J. 1973; 13: 23-30.

68. Marshall DW, Bentsen RG. A computer model to determine the temperature distributions in a wellbore. J Can Pet Technol. 1982; 21: 63-75.

69. Hanbury G, Vasquez VR. Life cycle analysis of geothermal energy for power and transportation: A stochastic approach. Renew Energy. 2018; 115: 371-381.

70. Sharma P, Al Saedi AQ, Kabir CS. Geothermal energy extraction with wellbore heat exchanger: Analytical model and parameter evaluation to optimize heat recovery. Renew Energ. 2020; 166: 1-8.

71. Al Saedi AQ, Sharma P, Kabir CS. A novel cyclical wellbore-fluid circulation strategy for extracting geothermal energy. Energy. 2021; 235: 121385.

72. Benavides J, Sharma P, Al Saedi AQ, Kabir CS. Techno-economic analysis of green energy resources for power generation & direct use by preserving near-wellbore geothermal gradient. Energy Sustain Dev. 2023; 74: 127-139.

73. Zhang Y, Yu C, Li G, Guo X, Wang G, Shi Y, et al. Performance analysis of a downhole coaxial heat exchanger geothermal system with various working fluids. Appl Therm Eng. 2019; 163: 114317.

74. Hu X, Banks J, Wu L, Liu WV. Numerical modeling of a coaxial borehole heat exchanger to exploit geothermal energy from abandoned petroleum wells in Hinton, Alberta. Renew Energy. 2020; 148: 1110-1123.

75. Hashish RG, Zeidouni M. Injection profiling through temperature warmback analysis under variable injection rate and variable injection temperature. Transp Porous Media. 2021; 141: 107-149.

76. Hashish RG, Zeidouni M. Analysis of warm-back data after cold-fluid injection into multilayer reservoirs. SPE Res Eval Eng. 2019; 23: 212-229.

77. Hashmi GM, Hasan AR, Kabir CS. Simplified modeling of plunger-lift assisted production in gas wells. J Nat Gas Sci Tech. 2018; 52: 454-460.

78. Xiang Z, Kabir CS. Simplified transient-IPR modeling in intermittent gas-lift and plunger-lift systems. J Pet Sci Eng. 2019; 179: 31-43.

79. Kar T, Naderi K, Firoozabadi A. Asphatene deposition and removal in flowlines and mitigation by effective functional molecules. SPE J. 2020; 25: 771-787.

80. Qi M, Moghantoo RG, Su X, Li M. An integrated simulation approach for wellbore blockage considering precipitation, aggregation, and deposition of asphaltene particles. SPE J. 2021; 26: 3151-3166.

81. Kabir CS, Jamaluddin AKM. Asphaltene characterization and mitigation in South Kuwait's Marrat reservoir. SPE Prod Oper. 2002; 17: 251-258.

82. White M, Pierce K, Acharya T. A review of wax formation/mitigation technologies in the petroleum industry. SPE Prod Oper. 2017; 33: 476-485.

83. Borden K. Flow assurance: Hydrates and paraffin management. Oil Gas Facil. 2015; 3: 29-33.

84. Ebeltoft H, Majeed Y, Sœrgärd E. Hydrate control during deepwater drilling: Overview and new drilling-fluids formulations. SPE Drill Complet. 2001; 16: 19-26.

85. Pickarts MA, Brown E, Delgado-Linares JG, Veedu V, Koh CA. A comprehensive investigation into the effect of a low surface energy treatment on gas hydrate, asphaltene, and wax formation, deposition, and adhesion. SPE J. 2022; 27: 410-421.

86. Parisi ML, Ferrara N, Torsello L, Basosi R. Life cycle assessment of atmospheric emission profiles of the Italian geothermal power plants. J Cleaner Prod. 2019; 234: 881-894.

87. Nogara J, Zarrouk S. Corrosion in geothermal environment: Part 1: Fluids and their impact. Renew Sustain Energy Rev. 2018; 282: 1333-1346.

88. Nogara J, Zarrouk S. Corrosion in geothermal environment: Part 2: Metals and alloys. Renew Sustain Energy Rev. 2018; 282: 1347-1369.